Quarterly Technical Report

Solid State Research
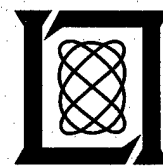
DTIC QUALITY INSPECTED 2

1996:3

Lincoln Laboratory

MASSACHUSETTS INSTITUTE OF TECHNOLOGY

LEXINGTON, MASSACHUSETTS

19970324 030

The ESC Public Affairs Office has reviewed this report, and it is releasable to the National Technical Information Service, where it will be available to the general public, including foreign nationals.

This technical report has been reviewed and is approved for publication.

FOR THE COMMANDER

Gary Tutungian
Administrative Contracting Officer
Contracted Support Management

MASSACHUSETTS INSTITUTE OF TECHNOLOGY
LINCOLN LABORATORY

SOLID STATE RESEARCH

QUARTERLY TECHNICAL REPORT

1 MAY–31 JULY 1996

ISSUED 12 MARCH 1997

LEXINGTON   MASSACHUSETTS

ABSTRACT

This report covers in detail the research work of the Solid State Division at Lincoln Laboratory for the period 1 May through 31 July 1996. The topics covered are Quantum Electronics, Electrooptical Materials and Devices, Submicrometer Technology, High Speed Electronics, Microelectronics, Analog Device Technology, and Advanced Silicon Technology. Funding is provided primarily by the Air Force, with additional support provided by the Army, DARPA, Navy, BMDO, NASA, and NIST.

TABLE OF CONTENTS

LIST OF ILLUSTRATIONS

LIST OF ILLUSTRATIONS (Continued)

LIST OF ILLUSTRATIONS (Continued)

LIST OF TABLES

INTRODUCTION

1. QUANTUM ELECTRONICS

The unfocused 157-μJ output from a high-power passively Q-switched microlaser has been used to drive periodically poled lithium niobate optical parametric amplifiers at wavelengths between 1.4 and 4.4 μm. With a peak conversion efficiency of nearly 100%, these devices generate 100-kW, subnanosecond pulses in the mid infrared, with a beam quality that is better than 2 times diffraction limited.

A 946-nm diode-pumped passively Q-switched Nd:YAG microlaser has been constructed from a 1.2-mm-thick piece of Nd:YAG diffusion bonded to a 0.21-mm-thick piece of Cr^{4+}:YAG. When pumped with a 1-W fiber-coupled diode laser, it has produced a 30-kHz train of single-frequency, TEM$_{00}$ pulses, with a pulse width of 10 ns (full width at half-maximum) and a pulse energy of 0.6 μJ.

2. ELECTROOPTICAL MATERIALS AND DEVICES

Near-bandedge resonant enhancement in the third-order nonlinearity in passive InGaAsP/InP quantum-well waveguides has been used to implement wavelength shifters based on four-wave mixing. At 1.5-μm wavelength approximately –20-dB conversion efficiency was obtained with ~ 18-dBm CW pump power, and the conversion efficiency was nearly constant for wavelength shifts up to ~ 26 nm (3.3 THz), limited by the phase-matching bandwidth of the 8.5-mm-long device.

A model has been developed for the periodic strain field near the wafer fusion interface of lattice-mismatched single crystals. The model predicts highly localized strain and is consistent with the experimental observations of nearly defect-free material except at the interface.

GaSb epilayers have been grown on GaAs substrates by organometallic vapor phase epitaxy using either a single- or two-step procedure. For growth temperatures of 550 and 580°C both procedures have yielded epilayers with similar electrical and structural properties, but for growth temperatures above 580°C the two-step procedure provided significantly better properties.

Strained-quantum-well diode lasers consisting of compressively strained InAsSb active layers and tensile-strained InAlAsSb barrier layers have exhibited cw power of 215 mW/facet at 80 K. The internal quantum efficiency and internal loss coefficient at 80 K are estimated to be 63% and 9 cm^{-1}, respectively.

3. SUBMICROMETER TECHNOLOGY

Laser-induced microchemical etching of silicon has been developed to machine waveguide structures for the terahertz operating regime. This technique uses a thermally activated chemical reaction to etch three-dimensional patterns with a lateral resolution of 1 μm.

A high-speed optical sampling system for electrical signals has been developed using a mode-locked laser and Mach-Zehnder interferometer. Signal processing techniques were used to linearize the modulator and thereby implement an analog-to-digital converter with 78-dB spur-free dynamic range.

4.   HIGH SPEED ELECTRONICS

A device has been invented that has a large potential impact for electronic displays. The device is a light valve, which we are calling a microshutter, and has a fundamentally simple electromechanical structure that is easy to make and has been shown to be highly reliable.

5.   MICROELECTRONICS

Monolithic arrays of silicon avalanche photodiodes for visible (532 nm) Geiger-mode operation have been fabricated for use in imaging laser radar systems that will have subnanosecond timing resolution and single-photon-per-pixel sensitivity. Dark count rates as low as 3 Kcounts/s have been observed at room temperature at a bias 4 V above breakdown.

6.   ANALOG DEVICE TECHNOLOGY

Critical subcircuits of a superconductive 2-gigachip-per-second spread-spectrum modem have been demonstrated. These circuits were fabricated using a new doubly planarized all-refractory technology for superconductors (DPARTS) process.

7.   ADVANCED SILICON TECHNOLOGY

A self-aligned cobalt silicide process has been developed to make good contacts to devices such as quarter-micrometer transistors. The performance of quarter-micrometer transistors built in an ultrathin silicon film can be seriously degraded by the resistance of the contacts to source and drain.

REPORTS ON SOLID STATE RESEARCH

1 MAY THROUGH 31 JULY 1996

PUBLICATIONS

Progress in 193-nm Positive Resists	R. D. Allen* R. Sooriyakumaran* J. Optiz* G. M. Wallraff* G. Breyta* R. A. DiPietro* R. R. Kunz U. Okoroanyanwu* C. G. Willson*	*J. Photopolym. Sci. Technol.* **9**, 465 (1996)
Protecting Groups for 193-nm Photoresists	R. D. Allen* R. Sooriyakumaran* J. Optiz* G. M. Wallraff* R. A. DiPietro* G. Breyta* D. C. Hofer* R. R. Kunz S. Jayaraman* R. Shick* B. Goodall* U. Okoroanyanwu* C. G. Willson*	*Proc. SPIE* **2724**, 334 (1996)

---

*Author not at Lincoln Laboratory.

High Power Failure of Superconducting Microwave Filters: Investigation by Means of Thermal Imaging	G. Hampel* P. Kolodner* P. L. Gammel* P. A. Polakos* E. deObaldia* P. M. Mankiewich* A. Anderson R. Slattery D. Zhang* G. C. Liang* C. F. Shih*	*Appl. Phys. Lett.* **69**, 571 (1996)
Reflective Linearized Modulator	G. E. Betts F. J. O'Donnell K. G. Ray D. K. Lewis* D. E. Bossi* K. Kissa* G. W. Drake*	*Integrated Photonics Research, OSA Technical Digest Series*, Vol. 6 (Optical Society of America, Washington, D.C., 1996), p. 626
Effects of Low-Temperature-Grown GaAs and AlGaAs on the Current of a Metal-Insulator-Semiconductor Structure	C. L. Chen L. J. Mahoney K. B. Nichols M. J. Manfra E. R. Brown P. M. Nitishin K. M. Molvar B. F. Gramstorff R. A. Murphy	*J. Vac. Sci. Technol. B* **14**, 1745 (1996)
Generalized Effective Index Series Solution Analysis of Waveguide Structures with Positionally Varying Refractive Index Profiles	J. P. Donnelly S. D. Lau	*IEEE J. Quantum Electron.* **32**, 1070 (1996)

---

*Author not at Lincoln Laboratory.

Diode-Pumped Solid-State Lasers	T. Y. Fan	In *New Perspectives in Laser Sources and Applications*, A. Miler and D. M. Finlayson, eds. (Institute of Physics Publishing, Philadelphia, 1996), p. 163
Comparison of Electric Field Emission from Nitrogen-Doped, Type Ib Diamond, and Boron-Doped Diamond	M. W. Geis J. C. Twichell N. N. Efremow K. Krohn T. M. Lyszczarz	*Appl. Phys. Lett.* **68**, 2294 (1996)
Diamond Emitters Fabrication and Theory	M. W. Geis J. C. Twichell T. M. Lyszczarz	*J. Vac. Sci. Technol. B* **14**, 2060 (1995)
Electronic and Structural Properties of GaN Grown by Hydride Vapor Phase Epitaxy	W. Götz* L. T. Romano* B. S. Krusor* N. M. Johnson* R. J. Molnar	*Appl. Phys. Lett.* **69**, 242 (1996)
High Thermoelectric Figures of Merit in PbTe Quantum Wells	T. C. Harman D. L. Spears M. J. Manfra	*J. Electron. Mater.* **25**, 1121 (1996)
Experimental Study of the Effect of Quantum-Well Structures on the Thermoelectric Figure of Merit	L. D. Hicks* T. C. Harman X. Sun* M. S. Dresselhaus*	*Phys. Rev. B* **53**, R10 493 (1996)
Multipass Optical Parametric Amplifier	T. H. Jeys	*Opt. Lett.* **21**, 1229 (1996)
Properties of Photoresist Polymers	R. R. Kunz	In *Physical Properties of Polymers Handbook*, J. E. Mark, ed. (AIP Press, Woodbury, N.Y., 1996), p. 637

*Author not at Lincoln Laboratory.

High Resolution Studies of Crystalline Damage Induced by Lapping and Single-Point Diamond Machining of Si(100)	R. R. Kunz H. R. Clark P. M. Nitishin M. Rothschild B. S. Ahern*	*J. Mater. Res.* **11**, 1228 (1996)
Limits to Etch Resistance for 193-nm Single-Layer Resists	R. R. Kunz S. C. Palmateer A. R. Forte R. D. Allen* G. M. Wallraff* R. A. DiPietro* D. C. Hofer*	*Proc. SPIE* **2724**, 365 (1996)
High-Power Diode-Laser-Pumped Midwave Infrared HgCdTe/CdZnTe Quantum Well Lasers	H. Q. Le A. Sanchez J. M. Arias* M. Zandian* R. R. Zucca* Y.-Z. Liu*	*Proceedings of the 7th International Conference on Narrow Gap Semiconductors* (Institute of Physics Publishing, Philadelphia, 1995), p. 24
High-Temperature Superconductive Wideband Compressive Receivers	W. G. Lyons D. R. Arsenault A. C. Anderson T. C. L. G. Sollner P. G. Murphy M. M. Seaver R. R. Boisvert R. L. Slattery R. W. Ralston	*IEEE Trans. Microwave Theory Tech.* **44**, 1258 (1996)
Dry Development of Sub-0.25 μm Features Patterned with 193 nm Silylation Resist	S. C. Palmateer A. R. Forte R. R. Kunz M. W. Horn	*J. Vac. Sci. Technol. A* **14**, 1132 (1996)

---

*Author not at Lincoln Laboratory.

Evaluation of Materials for 193-nm Lithography	U. Schaedeli* E. Tinguely* K. Cherubini* B. Maire* A. Blakeney* P. Falcigno* R. R. Kunz	*J. Photopolym. Sci. Technol.* **9**, 435 (1996)
Bilayer Resist Approach for 193-nm Lithography	U. Schaedeli* E. Tinguely* A. J. Blakeney* P. Falcigno* R. R. Kunz	*Proc. SPIE* **2724**, 344 (1996)
Laser Linking of Metal Interconnects: Analysis and Design Considerations	Y-L. Shen* S. Suresh* J. B. Bernstein	*IEEE Trans. Electron Devices* **43**, 402 (1996)
Semiconductor Amplifiers and Lasers with Tapered Gain Regions	J. N. Walpole	*Opt. Quantum Electron.* **28**, 623 (1996)

ACCEPTED FOR PUBLICATION

Use of CCD Imagers for Charged-Particle Spectroscopy	B. E. Burke T. H. Hotaling R. D. Petrasso* C. Li*	*Rev. Sci. Instrum.*
High CW Power (> 200 mW/Facet) at 3.4 μm from InAsSb/InAlAsSb Strained Quantum-Well Diode Lasers	H. K. Choi G. W. Turner M. J. Manfra	*Electron. Lett.*
High-Power 1.3 μm InGaAsP/InP Amplifiers with Tapered Gain Regions	J. P. Donnelly J. N. Walpole G. E. Betts S. H. Groves	*IEEE Photon. Technol. Lett.*

---

*Author not at Lincoln Laboratory.

Diamond Emitters Fabrication and Theory	M. W. Geis J. C. Twichell T. M. Lyszczarz	*Lincoln Lab. J.*
Calorimetric Measurements of Optical Materials for 193 nm Lithography	A. Grenville R. Uttaro J. H. C. Sedlacek M. Rothschild D. Corliss	*J. Vac. Sci. Technol. B*
Plasma-Deposited Silylation Resist for 193-nm Lithography	M. W. Horn B. E. Maxwell R. B. Goodman R. R. Kunz L. M. Eriksen	*J. Vac. Sci. Technol. B*
Status of 193-nm Lithography Development at Lincoln Laboratory	R. R. Kunz J. A. Burns S. G. Cann C. L. Keast M. W. Horn S. C. Palmateer M. Rothschild D. C. Shaver	*Jpn. J. Appl. Phys.*
Light Scattering in High-Dislocation-Density GaN	Z. L. Liau R. L. Aggarwal P. A. Maki R. J. Molnar J. N. Walpole R. C. Williamson I. Melngailis	*Appl. Phys. Lett.*
High Performance CCD Imager Technology for Plasma Diagnostics	R. K. Reich W. M. McGonagle J. A. Gregory R. W. Mountain B. B. Kosicki E. D. Savoye	*Rev. Sci. Instrum.*

How Practical Is 193-nm Lithography?	M. Rothschild J. H. C. Sedlacek S. Schenker* W. G. Oldham* A. Grenville	*J. Vac. Sci. Technol. B*
Binary Optics: A VLSI-Based Microoptics Technology	M. B. Stern	*Microelectron. Eng.*
Antimonide-Based Mid-Infrared Quantum-Well Diode Lasers	G. W. Turner H. K. Choi	In *Optoelectrical Properties of* *Semiconductor Quantum* *Wells and Superlattices,* M. O. Manasreh, ed. (Gordon and Breach, Langhorne, Pa.)
Diffraction-Limited 1.3 μm Wavelength Tapered-Gain-Region Lasers with Over 1 W CW Output Power	J. N. Walpole J. P. Donnelly S. H. Groves L. J. Missaggia J. D. Woodhouse* R. J. Bailey A. Napoleone	*IEEE Photon. Technol. Lett.*
Methyl- and Ethyl-Based Organometallic Sources for GaSb Growth	C. A. Wang	*Metalorganic News*
Lattice-Matched GaSb/AlGaSb Double-Heterostructure Diode Lasers Grown by OMVPE	C. A. Wang H. K. Choi	*Electron. Lett.*

---

*Author not at Lincoln Laboratory.

PRESENTATIONS[†]

Hydride Vapor Phase Epitaxy of Gallium Nitride Thick Films for Quasi-Bulk Substrates	R. Molnar	1996 Electrochemical Society Meeting, Los Angeles, California, 6 May 1996
Diamond Electronics	M. W. Geis	Lincoln Laboratory Technical Seminar Series, University of Michigan, Ann Arbor, Michigan, 8 May 1996
Use of Large-Area CCD Imagers for Charged-Particle Spectroscopy	B. E. Burke T. C. Hotaling R. D. Petrasso* C. Li*	High-Temperature Plasma Diagnostics Conference, Monterey, California, 12-16 May 1996
High Performance CCD Imager Technology for Plasma Diagnostics	R. K. Reich W. M. McGonagle J. A. Gregory R. W. Mountain B. B. Kosicki E. D. Savoye	
193-nm Optical Lithography for Sub-0.2-μm Device Fabrication	M. Rothschild	Technical Seminar, Finle Technologies, Waltham, Massachusetts, 16 May 1996
Gated-Field-Emitter Cathodes for Microwave Tubes	R. A. Murphy M. A. Hollis C. Bozler D. Rathman C. Harris	Microwave Power Tube Conference, Monterey, California, 21-23 May 1996
Electron Emission from Diamond	M. W. Geis J. C. Twichell T. M. Lyszczarz	Lincoln Laboratory Technical Seminar Series, University of Arizona, Tucson, Arizona, 22 May 1996

*Author not at Lincoln Laboratory.

[†]Titles of presentations are listed for information only. No copies are available for distribution.

193-nm Optical Lithography for Sub-0.2-μm Device Fabrication	M. Rothschild J. H. C. Sedlacek S. Schenker* W. G. Oldham* A. Grenville	Electron, Ion, Photon Beam Technology and Nanofabrication 1996, Atlanta, Georgia, 28-31 May 1996
Plasma-Deposited Silylation Resist for 193-nm Lithography	M. W. Horn B. E. Maxwell R. B. Goodman R. R. Kunz L. M. Eriksen	
High-Power 1.3 μm InGaAsP/InP Lasers and Amplifiers with Tapered Gain Regions	J. P. Donnelly J. N. Walpole G. E. Betts S. H. Groves J. D. Woodhouse* L. J. Missaggia F. J. O'Donnell R. J. Bailey	1996 Conference on Lasers and Electro-Optics, Anaheim, California, 2-7 June 1996
Nonlinear Frequency Conversion with Passively Q-Switched Microchip Lasers	J. J. Zayhowski	
Diamond Cold Cathodes	M. W. Geis J. C. Twichell T. M. Lyszczarz K. E. Krohn N. N. Efremow C. A. Marchi	23rd IEEE International Conference on Plasma Science, Boston, Massachusetts, 3-5 June 1996
OMVPE Growth of AlSb-Based Alloys	C. A. Wang	8th International Conference on Metal Organic Vapour Phase Epitaxy, Cardiff, Wales, 9-13 June 1996
Characteristics of GaSb Growth Using Various Gallium and Antimony Precursors	C. A. Wang S. Salim* K. F. Jensen* A. C. Jones*	

---

*Author not at Lincoln Laboratory.

A Novel Packaging Material System for High Temperature Electronics	D. Rathman J. Haggerty* A. Lightfoot* W. Robbins*	3rd International High Temperature Electronics Conference, Albuquerque, New Mexico, 9-14 June 1996
Tapered Semiconductor Diode Optical Power Amplifier and Oscillator	J. N. Walpole	Lincoln Laboratory Technical Seminar Series, Tufts University, Medford, Massachusetts, 17 June 1996
High-Performance CCD Imagers for Low-Light-Level Applications	J. A. Gregory	Annual Symposium of the New England Chapter, American Vacuum Society, Burlington, Massachusetts, 17-18 June 1996
Semiconductor Process and Device Development at MIT Lincoln Laboratory	J. A. Gregory	
Antimonide-Based Strained Quantum-Well Diode Lasers	H. K. Choi G. W. Turner	17th Nordic Semiconductor Meeting, Trondheim, Norway, 17-20 June 1996
Cylindrical Magnetron Sputtering of YBCO Thin Films	A. C. Anderson	Strategic Analysis Meeting, Arlington, Virginia, 20 June 1996
Linearized Electro-optic Modulators	G. E. Betts	1996 IEEE MTT-S International Microwave Symposium, San Francisco, California, 21 June 1996

---

*Author not at Lincoln Laboratory.

Electron Emission from Diamond	M. W. Geis J. C. Twichell T. M. Lyszczarz	
193-nm Optical Lithography for Sub-0.2-μm Device Fabrication	M. Rothschild J. H. C. Sedlacek S. Schenker* W. G. Oldham* A. Grenville	Gordon Research Conference, Hennicker, New Hampshire, 23-28 June 1996
Evaluation of Materials for 193-nm Lithography	U. Schaedeli* E. Tinguely* A. Blakeney* P. Falcigno* R. R. Kunz	Japan Photopolymer Conference, Tokyo, Japan, 26-28 June 1996
Progress Toward a Twystrode with a Gated FEA Cathode	R. A. Murphy M. A. Hollis C. Bozler D. Rathman C. Harris	IEEE International Conference on Plasma Science, Boston, Massachusetts, 30 June 1996
Electron Emission from Diamond	M. W. Geis J. C. Twichell T. M. Lyszczarz	International Vacuum Electron Source Conference, Eindhoven, The Netherlands, 1-4 July 1996

*Author not at Lincoln Laboratory.

193-nm Optical Lithography for Sub-0.2-μm Device Fabrication	R. R. Kunz	
Status of 193-nm Lithography Development at Lincoln Laboratory	R. R. Kunz J. A. Burns S. G. Cann C. L. Keast M. W. Horn S. C. Palmateer M. Rothschild D. C. Shaver	Microprocess Conference '96, Kita-Kyushu, Japan, 8-11 July 1996
An Optical Correlator Using a Low-Temperature-Grown GaAs Photoconductor	S. Verghese E. Brown N. Zamdmer* Q. Hu*	Progress in Electromagnetics Research Symposium, Innsbruck, Austria, 8-12 July 1996
Semiconductor Lasers, Microoptics and Integrated Optoelectronics: Innovations Through Material and Fabrication Technologies	Z-L. Liau	Lincoln Laboratory Technical Seminar Series, University of California, Los Angeles, California, 18 July 1996
Characterization of the Electrical Properties of GaN Grown by Hydride Vapor Phase Epitaxy	W. Götz* L. T. Romano* J. Walker* N. M. Johnson* R. J. Molnar	23rd International Conference on the Physics of Semiconductors, Berlin, Germany, 21-26 July, 1996

*Author not at Lincoln Laboratory.

*Author not at Lincoln Laboratory.

ORGANIZATION

SOLID STATE DIVISION

D. C. Shaver, *Head*
I. Melngailis, *Associate Head*
R. W. Ralston, *Associate Head*
J. F. Goodwin, *Assistant*

A. L. McWhorter, *Fellow*
D. Abusch-Magder, *Research Assistant*
J. T. Chiou, *Research Assistant*
J. P. Mattia, *Research Assistant*
N. L. DeMeo, Jr., *Associate Staff*
J. W. Caunt, *Assistant Staff*
K. J. Challberg, *Administrative Staff*
J. D. Pendergast, *Administrative Staff*

SUBMICROMETER TECHNOLOGY

M. Rothschild, *Leader*
T. M. Lyszczarz, *Assistant Leader*
L. H. Dubois, *Senior Staff*[†]

Astolfi, D. K.	Krohn, K. E.
Bloomstein, T. M.	Kunz, R. R.
Craig, D. M.	Maki, P. A.
DiNatale, W. F.	Palmacci, S. T.
Doran, S. P.	Palmateer, S. C.
Efremow, N. N., Jr.	Reinold, J. H., Jr.
Forte, A. R.	Sedlacek, J. H. C.
Geis, M. W.	Stern, M. B.
Goodman, R. B.	Twichell, J. C.
Hartney, M. A.	Uttaro, R. S.
Horn, M. W.	

QUANTUM ELECTRONICS

A. Sanchez-Rubio, *Leader*
T. Y. Fan, *Assistant Leader*

Aggarwal, R. L.	Jeys, T. H.
Cook, C. C.	Le, H. Q.
Daneu, V.	Ochoa, J. R.
DiCecca, S.	Zayhowski, J. J.
Dill, C., III	

ELECTROOPTICAL MATERIALS AND DEVICES

B. Y. Tsaur, *Leader*
D. L. Spears, *Assistant Leader*
R. C. Williamson, *Senior Staff*

Bailey, R. J.	Herrmann, F. P.	Nitishin, P. M.
Betts, G. E.	Iseler, G. W.	O'Donnell, F. J.
Chen, C. K.	Krohn, L., Jr.	Paul, S. A.*
Choi, H. K.	Liau, Z. L.	Poillucci, R. J.
Connors, M. K.	Manfra, M. J.	Reeder, R. E.
Cronin, S.*	Missaggia, L. J..	Santiago, D. D.
Donnelly, J. P.	Mull, D. E.	Turner, G. W.
Goodhue, W. D.	Napoleone, A.	Walpole, J. N.
Groves, S. H.	Nee, P.*	Wang, C. A.
Harman, T. C.		

---

* Research Assistant
[†] Intergovernmental Personnel Act assignment

HIGH SPEED ELECTRONICS

M. A. Hollis, *Leader*
E. R. Brown, *Assistant Leader*[†]
R. A. Murphy, *Senior Staff*

Bozler, C. O.	McIntosh, K. A.
Calawa, S. D.	McMahon, O. B.
Chen, C. L.	Molnar, R. J.
Harris, C. T.	Rabe, S.
Lincoln, G. A., Jr.	Rathman, D. D.
Mahoney, L. J.	Verghese, S.
Mathews, R. H.	Young, A. M.

ANALOG DEVICE TECHNOLOGY

T. C. L. G. Sollner, *Leader*
L. M. Johnson, *Assistant Leader*
A. C. Anderson, *Senior Staff*

Arsenault, D. R.	Macedo, E. M., Jr.
Boisvert, R. R.	McClure, D. W.
Brogan, W. T.	Murphy, P. G.
Feld, D. A.	Oates, D. E.
Fitch, G. L.	Sage, J. P.
Hamm, J. M.	Seaver, M. M.
Holtham, J. H.	Slattery, R. L.
Lyons, W. G.	

MICROELECTRONICS

E. D. Savoye, *Leader*
B. B. Kosicki, *Associate Leader*
B. B. Burke, *Senior Staff*

Aull, B. F.	Johnson, K. F.
Daniels, P. J.	Lind, T. A.
Doherty, C. L., Jr.	Loomis, A. H.
Dolat, V. S.	McGonagle, W. H.
Donahue, T. C.	Mountain, R. W.
Felton, B. J.	Percival, K. A.
Gregory, J. A.	Reich, R. K.
Hotaling, T. C.	Young, D. J.

ADVANCED SILICON TECHNOLOGY

C. L. Keast, *Leader*
P. W. Wyatt, *Associate Leader*
A. H. Anderson, *Senior Staff*

Berger, R.	Howard, J. F.
Burns, J. A.	Knecht, J. M.
Davis, P. V.	Liu, H. I.
D'Onofrio, R. P.	Newcomb, K. L.
Frankel, R. S.	Soares, A. M.
Fritze, M.	Wachtmann, B. K.
Herndon, T. O.	Young, G. R.

[†] Intergovernmental Personnel Act assignment

1. QUANTUM ELECTRONICS

1.1 PPLN OPTICAL PARAMETRIC AMPLIFIERS PUMPED BY HIGH-POWER PASSIVELY Q-SWITCHED MICROLASERS

Diode-pumped passively Q-switched Nd:YAG microlasers are compact, economical, all-solid-state sources of coherent, subnanosecond, multikilowatt pulses at high repetition rates [1]–[3]. The high intensities generated by these devices at 1.064 μm has led to efficient second-, third-, fourth-, and fifth-harmonic generation using a series of nonlinear optical crystals butt coupled to the laser without any intervening optics [2]–[4]. Most of the work reported on these devices has used a 1-W diode laser pump, and the optical frequencies generated without amplification of the microlaser output have been limited to harmonics of the 1.064-μm laser line. Recently, the amplified output of a passively Q-switched microlaser has been used to pump multipass KTP parametric amplifiers operating in the eyesafe spectral region near 1.5 μm [5]. The microlaser discussed in this paper is pumped by a fiber-coupled 12-W diode laser array [3]. The increased output power allows this device to directly pump periodically poled lithium niobate (PPLN) optical parametric amplifiers [3], making it possible to produce compact, inexpensive microlaser systems at any wavelength from the infrared to the ultraviolet.

The passively Q-switched microlaser used in all of the experiments discussed here consists of a 3-mm-thick piece of Nd:YAG, a 3-mm-thick piece of Cr^{4+}:YAG, and a 6-mm-thick piece of Nd:YAG, bonded together in that order. The Nd:YAG is doped at 1.1 at.% Nd; the Cr^{4+}:YAG has an unsaturated absorption coefficient of 1.5 cm^{-1} at 1.064 μm. All of the crystals have flat, parallel faces normal to the cavity axis. The unbonded side of the 3-mm-thick Nd:YAG is dielectrically coated to transmit the pump light and have a high reflectivity at 1.064 μm. The free side of the 6-mm-thick YAG is coated to be 40% transmitting at 1.064 μm.

The microlaser is longitudinally pumped with a fiber-coupled 12-W diode laser array. The output facet of the pump fiber (500-μm core diameter, NA = 0.22) is imaged into the 3-mm-thick Nd:YAG with a demagnification of ~ 2. All of the useful pump light is absorbed within this crystal. The purpose of the 6-mm-thick Nd:YAG is to increase the cavity length in a way that maintains the robustness of the device (undoped YAG would work as well as doped material). The increased cavity length results in a larger oscillating-mode diameter [6] and, therefore, more efficient use of the pump. The Cr^{4+}:YAG is positioned near the center of the cavity so that spatial hole burning within the saturable absorber has the largest possible effect on maintaining single-longitudinal-mode operation of the laser.

The diode laser pump array is operated in a pulsed mode, with the output power at either its maximum value or zero. The length of the pump pulse is adjusted to provide a single output pulse from the passively Q-switched laser for each diode pulse. At pulse repetition rates below 2 kHz, the microlaser produces 157 μJ in a single-frequency, TEM_{00} pulse. The full width at half-maximum (FWHM) of the pulse is 0.9 ns and the waist radius is 94 μm. At 2 kHz the duty cycle of the diode array is ~ 50%. At repetition rates > 2 kHz it becomes difficult to maintain single-mode performance of the device. All of the experiments discussed below were performed at repetition rates < 2 kHz.

1

The peak intensity of the unfocused output of the microlaser is 1 GW/cm^2; the confocal parameter is 5.2 cm. These parameters are well suited to pumping optical parametric devices. As a demonstration of this, a 13-mm-long piece of PPLN [7] was placed in the unfocused output beam of the laser, as shown in Figure 1-1. The PPLN was poled for quasi phase matching of the parametric conversion of 1.064-μm radiation to 1.59- and 3.22-μm radiation. It had flat, uncoated faces parallel to the domain walls and was oriented with these faces nearly normal to the pump beam. By aligning the faces slightly off normal with respect to the pump light, feedback into the pump laser was avoided. In addition, the possibility that the PPLN would oscillate was eliminated, forcing it to act as a single-pass parametric amplifier. The polarization of the microlaser was oriented for maximum parametric conversion in the PPLN.

With the assumption that the input to the parametric amplifier is 1 photon of 1.59-μm light, the threshold 1.064-μm pump intensity $I_{p,t}$ is given by

$$KI_{p,t} = \left[\frac{1}{2l}\ln\left(\frac{4\lambda_s E_{s,t}}{hc}\right)\right]^2 \quad , \tag{1.1}$$

where

$$K = \frac{8\pi^2 d_{\text{eff}}^2}{\varepsilon_0 c \lambda_s \lambda_i n_s n_i n_p} \quad . \tag{1.2}$$

In these equations, λ is wavelength, E is pulse energy, h is Planck's constant, c is the speed of light, d_{eff} is the effective nonlinear coefficient, ε_0 is the dielectric constant of free space, n is refractive index, the subscripts s, i, and p refer to the signal, idler, and pump frequencies, respectively, and the subscript t refers to the threshold value. For the experiment discussed above $\lambda_s = 1.59$ μm, $l_i = 3.22$ μm, $\lambda_p = 1.064$ μm, $n_s = 2.14$, $n_i = 2.09$, $n_p = 2.16$, and $l = 13$ mm. For perfect poling of the lithium niobate (LiNbO$_3$), $d_{\text{eff}} = 2d_{33}$(LiNbO$_3$)/π = 17 pm/V [7]. If we set the threshold condition at $E_{s,t} = 1$ μW, the calculated threshold intensity $I_{p,t}$ is 820 MW/cm^2.

286465-1

12-W FIBER-COUPLED DIODE LASER

LENS

Nd:YAG Cr^{4+}:YAG Nd:YAG

PPLN

OUTPUT

12 mm

32 mm

13 mm
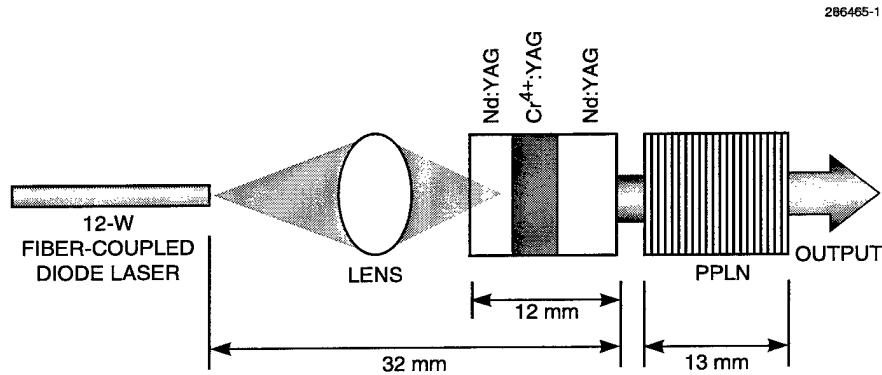
Figure 1-1. Experimental setup for optical parametric amplification of output of high-power passively Q-switched microlaser using periodically poled lithium niobate (PPLN).

2

In the experiment, with an incident pump intensity of 1 GW/cm^2, the PPLN was ~ 1.5 times above threshold, in reasonable agreement with theory. It converted 25% of the incident pump radiation to the signal and idler wavelengths. This corresponds to 26- and 12-μJ output pulses at 1.59 and 3.22 μm, respectively. Although the average conversion efficiency, determined by calorimetric measurements, was 25%, the peak of the input pulse was nearly 100% depleted, as shown in Figure 1-2. Similar conversion efficiencies and pump depletion have been observed with KTP parametric amplifiers [5].

The threshold for parametric conversion in PPLN is dependent on the polarization of the pump laser. By rotating the polarization of the microlaser with respect to the PPLN c axis, the amplifier was brought through threshold. As this was done, oscilloscope traces of the 1.064-μm radiation transmitted by the PPLN varied continuously between the top and center traces of Figure 1-2. Calorimetric measurements of the total optical power (1.064 + 1.59 + 3.22 μm) showed no change, indicating that all of the depleted pump appeared as output radiation at the longer wavelengths. The parametrically generated output had a full width at half-maximum of < 500 ps and was better than 2 times diffraction limited at both wavelengths. Pulse-to-pulse amplitude variations were $\pm$ 1%.

The PPLN parametric amplifier described above was operated for several hours at room temperature without noticeable degradation of its performance. A similar device that used PPLN obtained from a different source was also tested [3]. This device generated easily seen amounts of red, green, and blue radiation in addition to the longer-wavelength output, consistent with earlier observations of parametric oscillators [7]. The output quality and parametric conversion efficiency deteriorated after several minutes of use. The reason for the differences in the performance of the devices is not understood. It is known that the deterioration of the second device is a result of photorefractive damage caused by the visible light, which was not present in large amounts in the first device, and can be eliminated by heating the crystal [7]. If heating of the crystal is required, its impact on the final size and efficiency of the package must be considered.

Eight parametric amplifiers using 2-cm-long pieces of PPLN with poling periods uniformly spaced between 28 and 31 μm have been tested with the high-power microlaser. These devices oscillate with signal and idler wavelengths in the ranges 1.4–1.7 and 4.3–2.9 μm [7]. Each of these devices operated well in excess of threshold with properties similar to those of the first parametric amplifier discussed above.

Unlike the microlaser, which has a transform-limited bandwidth, the bandwidth of parametric amplifiers can be tens to hundreds of nanometers wide, determined by

$$\left| \left(\frac{n_p}{\lambda_p} - \frac{n_i(\lambda_i)}{\lambda_i} - \frac{n_s(\lambda_s)}{\lambda_s} - \frac{1}{\Lambda} \right)^2 - \frac{KI_p}{\pi^2} \right| l^2 \leq 1 \quad , \tag{1.3}$$

where Λ is the poling period in the PPLN. The 1.59-μm parametric amplifier discussed above has a calculated bandwidth of 60 nm; the bandwidth at 3.2 μm is 250 nm. A similar amplifier operating near degeneracy, 2.128 μm, would have an even larger bandwidth. While this may be disadvantageous for some applications, it offers potential advantages as well. For example, the broad bandwidth of these sources may make it possible to take absorption spectra with a single pulse, eliminating the need to tune

3
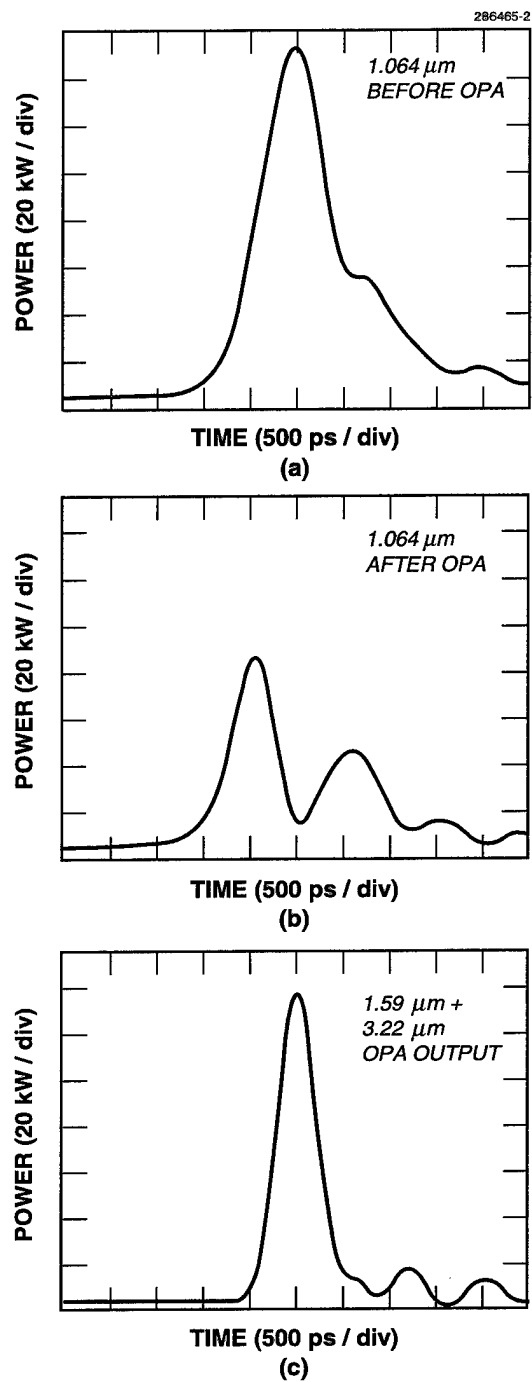
Figure 1-2. *(a) 1.064-μm input to a PPLN optical parametric amplifier (OPA), (b) 1.064-μm light transmitted by the parametric amplifier, and (c) sum of 1.59- and 3.22-μm light generated by the parametric amplifier. Fresnel losses have been subtracted from all traces. Oscillations on the trailing edge of the waveforms are due to electrical ringing in the detector. The bandwidth of the detection system was 1 GHz.*

4

the laser. It may also facilitate fluorescence spectroscopy by ensuring some overlap of the excitation pulse and narrow absorption features. In laser ranging systems, the broad bandwidth will reduce the effects of speckle.

The use of optical parametric amplifiers affords microlaser systems enormous wavelength flexibility. By using PPLN, parametric devices pumped by a high-power 1.064-μm microlaser can produce output at any wavelength between 1.35 and 5 μm. With unfocused power densities of hundreds of MW/cm^2, harmonic conversion of the output of the parametric amplifiers should be efficient, providing compact sources of high-peak-power, subnanosecond pulses at any wavelength from the mid infrared to the ultraviolet.

The high performance, compact size, and potential low cost of microchip parametric devices makes them attractive for industrial and field use. Potential applications include high-precision eyesafe ranging; time-resolved excitation, absorption, and fluorescence spectroscopy; multicolor three-dimensional imaging; and displays.

J. J. Zayhowski C. Dill III
J. L. Daneu   C. Cook

1.2 946-nm PASSIVELY Q-SWITCHED MICROLASER

A 946-nm diode-pumped passively Q-switched Nd:YAG microlaser was constructed from a 1.2-mm-thick piece of Nd:YAG diffusion bonded to a 0.21-mm-thick piece of Cr^{4+}:YAG. The Nd:YAG is doped at 1.8 at.% Nd; the Cr^{4+}:YAG has an unsaturated absorption coefficient of 0.35 cm^{-1} at 946 nm. All of the crystals have flat, parallel faces normal to the cavity axis. The unbonded side of the Nd:YAG is dielectrically coated to transmit the pump light and have a high reflectivity at 946 nm. The free side of the Cr^{4+}:YAG is coated to be 0.5% transmitting at 946 nm and 40% transmitting 1.064 μm in order to suppress laser oscillation at that frequency.

The microlaser was longitudinally pumped with an 808-nm fiber-coupled diode laser. The output facet of the pump fiber (100-μm core diameter, NA = 0.39) was butt coupled to the input face of the laser. When pumped with 1 W of optical power, at room temperature, the microlaser produced a 30-kHz train of 10-ns (FWHM) pulses, with a pulse energy of 0.6 μJ. The output pulses were single frequency and TEM$_{00}$. At this repetition rate there were pulse-to-pulse amplitude variations of several percent. At lower repetition rates (< 10 kHz) the pulse amplitudes became extremely stable.

These results constitute a proof-of-principle demonstration that Nd^{3+} microlasers operating in this wavelength range have the output energy, temporal waveform, and single-frequency performance needed for miniature time-of-flight water-vapor lidar systems. However, identification of appropriate overlaps of Nd^{3+} gain and water-vapor absorption lines is still needed.

J. J. Zayhowski T. Y. Fan
J. L. Daneu   C. Cook

REFERENCES

1. J. J. Zayhowski and C. Dill III, *Opt. Lett.* **19**, 1427 (1994).

2. J. J. Zayhowski, *Laser Focus World* (Penwell Publishing, Tulsa, Okla., 1996), p. 73.

3. Solid State Research Report, Lincoln Laboratory, MIT, 1996:2, p. 1.

4. J. J. Zayhowski, *Opt. Lett.* **21**, 588 (1996).

5. T. H. Jeys, *Opt. Lett.* **21**, 1229 (1996).

6. J. J. Zayhowski, *OSA Proc. Adv. Solid-State Lasers* **6**, 9 (1991).

7. L. E. Myers, R. C. Eckardt, M. M. Feyer, R. L. Byer, W. R. Bosenberg, and J. W. Pierce, *J. Opt. Soc. Am. B*, **12**, 2102 (1995).

2. ELECTROOPTICAL MATERIALS AND DEVICES

2.1 NONDEGENERATE FOUR-WAVE-MIXING WAVELENGTH CONVERSION IN LOW-LOSS PASSIVE InGaAsP/InP QUANTUM-WELL WAVEGUIDES

Wavelength conversion devices, which allow the transcription of information carried on one set of optical wavelengths onto another, are useful for wavelength-division-multiplexed optical networks. A common approach is to utilize nondegenerate four-wave mixing (FWM) in either semiconductor optical amplifiers [1]–[4] or dispersion-shifted silica fibers [5],[6]. Here, we describe FWM in passive InGaAsP/ InP quantum-well waveguides using the near-bandedge excitonic resonance nonlinearity [7]–[9] to generate a frequency-shifted conjugated output beam from pump and signal beams. Compared with FWM in active semiconductors, passive semiconductor devices require higher optical pump power, but are simpler, do not depend on free-carrier effects, and therefore have the potential advantage of simultaneous ultrahigh speed and broadband direct optical-to-optical conversion. Compared to silica fibers, semiconductors have several orders of magnitude lower latency, and have the potential for compact, monolithic integration.

In passive quantum-well waveguides, the third-order nonlinear susceptibility is enhanced near the bandedge because of quantum-well exciton resonance effects [7]–[9]. A figure of merit, which indicates the maximal conversion efficiency attainable with an optimal device length for a given pump frequency and pump-signal frequency detuning, is $|\chi^{(3)}|^2/[a^2 + \Delta\kappa^2]$, where α is the linear loss and $\Delta\kappa = \beta_2 \Delta n^2$ is the phase mismatch for group velocity dispersion β_2 and a pump-signal frequency detuning Δv. Optimum lengths in the loss-limited case are $\approx \ln(3)/\alpha$. The enhancement of the figure of merit near the excitonic edge results from $\chi^{(3)}$ increasing as $\sim 1/(v-v_{ex})^3$ while a and b_2 increase as $\sim 1/(v-v_{ex})^2$, where $(v-v_{ex})$ is the frequency offset from the excitonic resonance frequency. Projections indicate that CW conversion efficiencies of –10 dB with > 5-THz shift should be achievable at 1.55 μm in InGaAsP/InP quantum-well waveguides with $\leq$ 20-dBm pump power.

A key issue in achieving resonance enhancement of the figure of merit is the sharpness of the excitonic edge (narrow intrinsic linewidth) and the spatial uniformity of the excitonic resonance over a typical device length. The ability to grow uniform low-loss InGaAsP/InP quantum-well waveguide structures is thus crucial to developing passive FWM wavelength shifters. This requires highly uniform quantum wells with abrupt interfaces. Low-temperature photoluminescence linewidth, as shown in Figure 2-1, has been used as a measure of the quality of several different quantum-well structures for FWM applications. The use of quaternary InGaAsP quantum wells allows the independent optimization of quantum-well width and bandedge so as to minimize bandedge smearing due to monolayer variations in well thickness. As shown, 10-nm-thick InGaAsP quantum wells exhibited a narrower linewidth than the 6-nm-thick InGaAs wells. In both cases, the use of InP barriers instead of InGaAsP ($l_g \sim 1.1$ μm) barriers decreases the linewidth. The narrowest linewidth, ~ 7 meV, was obtained with 10-nm InGaAsP quantum wells and InP barriers.

7
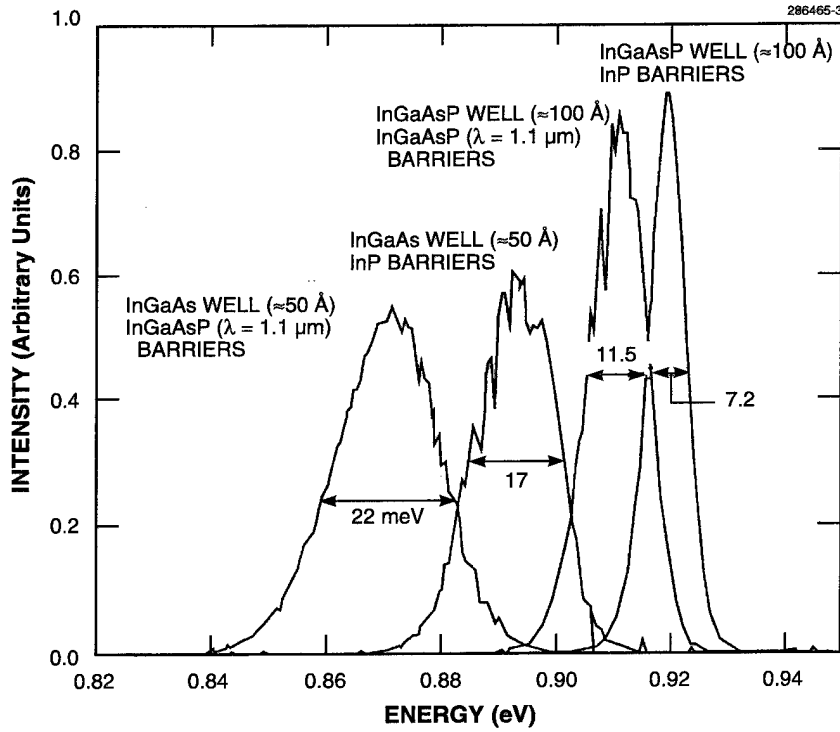
Figure 2-1. Low-temperature (T = 4.5 K) photoluminescence spectra of ternary InGaAs and quaternary InGaAsP quantum wells with wide-gap InGaAsP and InP barriers.

Initial FWM devices were therefore fabricated in material that contains a 10-nm InGaAsP quantum well with 10-nm InP barrier layers above and below it. For simplicity in understanding the physics of the nonlinearity, a single quantum well was employed in these initial experiments. The well and barriers are centered in an InGaAsP ($\lambda_g \sim 1.1$ μm) guiding layer. The bandedge of the quantum well was ~ 1.49 μm. The total thickness of the guiding region was ~ 4.7 μm. Unintentionally doped InP was used for the upper and lower cladding layers. These structures were grown on (100) n^+-InP substrates by organometallic vapor phase epitaxy.

Single-mode 2-μm-wide ridge waveguides, oriented in a (011) direction, were fabricated by a combination of dry and wet etching. The processed wafer was cleaved into test samples. Device lengths used in this initial evaluation were 7.5–10 mm. Low-power Fabry-Perot waveguide loss measurements indicate losses as low as 1–2 dB/cm at 1.55 μm. Transmission measurements indicated a sharp bandedge. For FWM measurements, the waveguide facets were coated with broadband antireflection coatings.

FWM wavelength conversion in these single-quantum-well devices was evaluated at room temperature under CW operating conditions using tunable external-cavity diode lasers with erbium-doped fiber amplifiers (EDFA) to provide the pump and input signal. Signal powers were generally kept at least 10-dB smaller than the pump power. For fixed wavelength shifts of ~ 10 nm (1.25 THz) with both pump

8

and signal polarized in the plane of the quantum well (TE polarization), CW conversion efficiencies of ≥ -22 dB were observed on an 8.5-mm-long device over the EDFA band with ~ 60-mW pump power coupled into the guide. Similar conversion efficiency was obtained with the signal on the high-energy and low-energy side of the pump. The highest conversion efficiency observed was approximately –20 dB, which was obtained with the pump at 1536 nm. For the pump fixed near the center of the EDFA band (~ 1.55 μm), the conversion efficiency was essentially constant for wavelength shifts up to ~ 26 nm (3.3 THz). This is consistent with dispersion calculations which indicate a dispersion-limited bandwidth of about this magnitude. A typical output spectrum of an 8.5-mm-long device is shown in Figure 2-2.

The magnitude of the mode-average effective $|\chi^{(3)}|$ of this device at 1540 nm determined from low-pump-power measurements is ~ 4.2×10^{-10} esu (5.9×10^{-14} cm^2/V), which corresponds to a self-phase n_2 value of -1.4×10^{-12} cm^2/W, assuming a two-photon absorption coefficient of 33 cm/GW. The cross-phase n_2 value at the signal frequency due to the strong pump is twice the self-phase value. The conversion efficiency for the 8.5-mm device vs pump power including two-photon absorption effects was calculated using the $|\chi^{(3)}|$ value determined from the low-power results and is shown as the solid curve in Figure 2-3. The calculation indicates that the measured conversion efficiency with 60-mW CW pump power is at least 6-dB lower than expected. Preliminary short-pulse low-average-power measurements did not show the same anomalous pump-power saturation effects as the CW measurements [10]. A measurement of CW pump transmission vs its power indicates a CW power-dependent loss that is greater than

286465-4
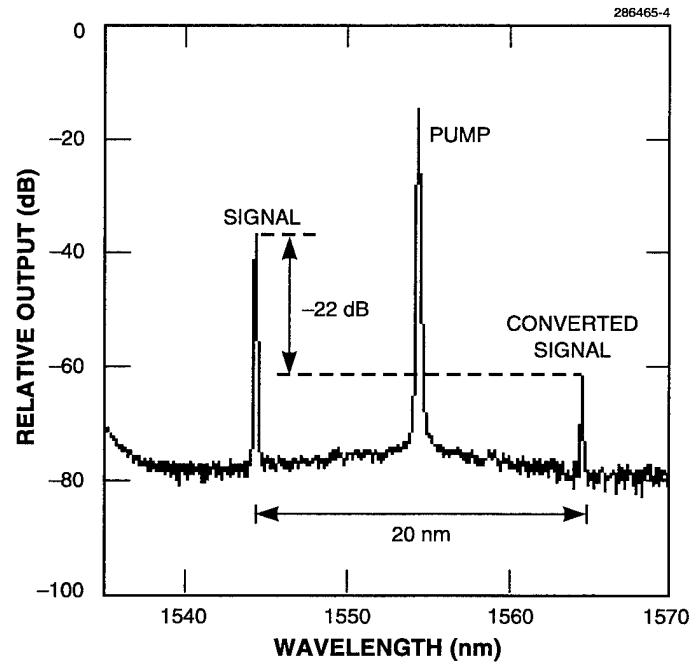
Figure 2-2. Typical CW output spectra of four-wave mixing in 8.5-mm-long InGaAsP/InP single-quantum-well waveguide.

9
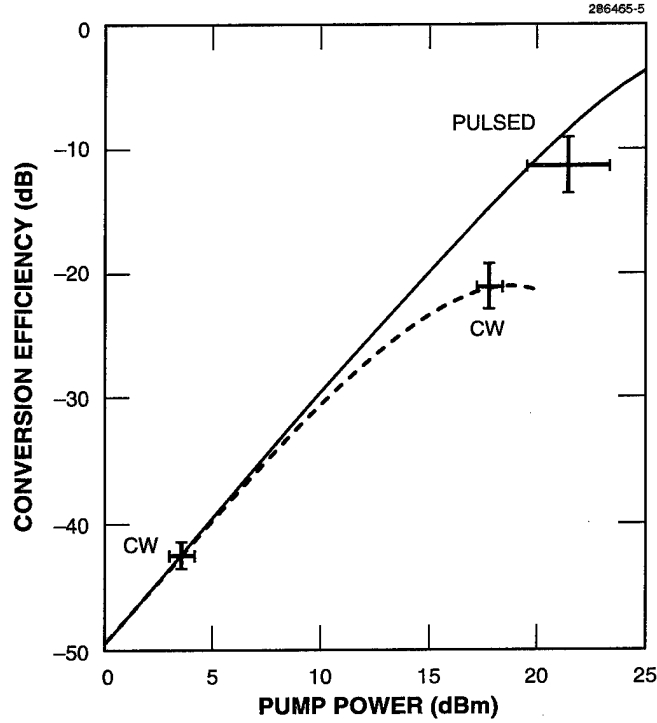
Figure 2-3. Conversion efficiency at 1540 nm as a function of pump power in an 8.5-mm-long device. The solid curve is the calculated conversion efficiency using the $|\chi^{(3)}|$ value obtained from the low-power CW measurement and includes two-photon absorption effects. The dashed curve indicates calculated conversion efficiency including an additional power-dependent loss of βP_{pump}.

that expected from two-photon absorption. This loss mechanism can be phenomenologically modeled with an expression for the loss coefficient $\alpha' = \alpha + P_{pump}\beta$, where P_{pump} is the input pump power and β is a coefficient. A β of 20 cm^{-1}/W is consistent with the transmission measurements, and its inclusion in the conversion efficiency calculation yields the dashed curve shown in Figure 2-3.

A possible explanation of the difference between CW and pulsed results is additional free-carrier loss due to the accumulation of photogenerated carriers under high-average-power operating conditions. Both two-photon and fundamental absorption contribute to carrier generation. Transmission measurements of a low-power probe beam vs λ — with and without the presence of a high-power 1.55-μm pump beam — and transient transmission measurements at the beginning of a long fast-risetime pulse both support the hypothesis that the enhanced absorption at high CW pump powers is due to the accumulation of photogenerated free carriers and not thermal effects. Since these carriers accumulate on a carrier lifetime timescale (~ 5 ns), it should be possible in more advanced device structures to sweep out these carriers with a weak electric field before they can accumulate.

10

Increases in conversion efficiency should be possible through further improvements in device design and fabrication. In addition to developing structures in which two-photon-generated free carriers can be swept out before they accumulate, the use of uniform multiple-quantum-well devices should result in higher performance, since the quantum-well resonance enhancement scales as the number of quantum wells while two-photon absorption and other parasitic losses do not. Shifting the bandedge 10- to 15-nm closer to the EDFA band should also increase the figure of merit of these devices at EDFA wavelengths by allowing more optimum use of the quantum-well exciton resonance. Optimization of the device length for a particular pump-frequency range and maximum wavelength shift is another consideration for maximizing performance.

J. P. Donnelly   S. H. Groves

H. Q. Le   A. Darwish

E. A. Swanson   E. I. Ippen

2.2 STRAINED INTERFACE OF LATTICE-MISMATCHED WAFER FUSION

Considerable interest has existed recently in a "wafer fusion" process in which single-crystal wafers are pressed together at elevated temperatures for the formation of covalent bonds along the interface [11]–[16]. The process is similar to sintering but occurs over a larger area. The process allows grown single-crystal layers to be transferred and monolithically integrated onto a substrate of a different lattice parameter or of a different crystal orientation to form novel optoelectronic devices. Except at the interface, virtually no dislocations have been found in the wafer-fused materials [12],[16], in sharp contrast with the direct heteroepitaxial growth of the materials on lattice-mismatched substrates [17],[18]. This has led to high-performance devices with good reliability [12]–[16]. One example of these rather interesting applications is the practical manufacturing of highly efficient AlGaInP light-emitting diodes, in which a transparent GaP substrate is wafer fused to replace the absorbing GaAs [15]. However, considerable strain is still present near the wafer fusion interface and needs to be examined to better understand the nature of the interface and to facilitate further device applications.

Several groups have obtained high-resolution transmission electron microscope cross-sectional views of the GaAs/InP wafer-fused interface and have observed an array of misfit dislocations along the interface with a regular spacing as expected from the amount of lattice mismatch [12],[16]. Based on this observation, we have developed a comprehensive model of the strain field near the interface. We consider the periodic compressive and tensile strains along the interface and describe a solution that satisfies the mechanical equilibrium and the boundary conditions. The model shows that the strain is highly localized to the interface and is consistent with the experimental observations of virtually defect-free materials and reliable high-performance devices.

The present model of lattice-mismatched wafer fusion is illustrated in Figure 2-4. The lattice parameters of the upper and lower wafers are a and $(1 + \varepsilon)a$, respectively, and the x- and z-axes are parallel and perpendicular to the interface, respectively. This simple two-dimensional case is considered

11
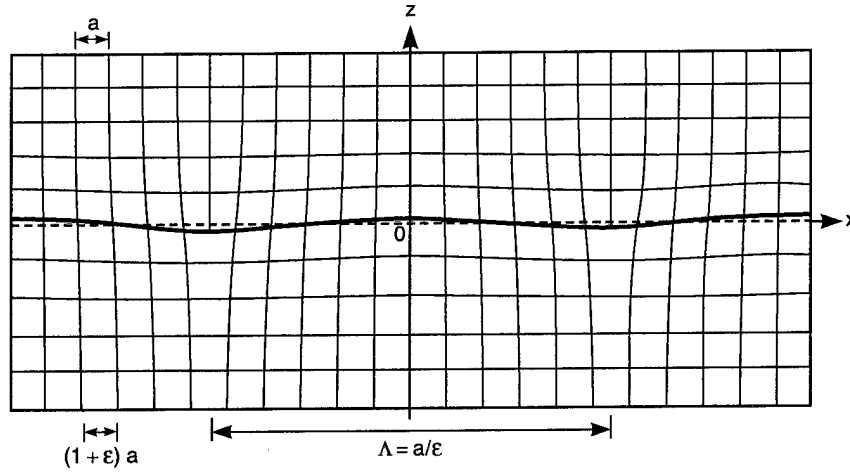
Figure 2-4. Schematic drawing of the present model of the interface of lattice-mismatched wafer fusion. The mismatch results in a periodic array of misfit dislocations. The strain field can be found by solving the elastic mechanical equilibrium equations for the given boundary conditions. The model reveals a wavy atomic displacement perpendicular to the interface. It also shows that the strain field is highly localized to a thin region along the interface.

first, and an extension to the more realistic three-dimensional case will be given later. The lattice mismatch ε is usually a few percent and gives rise to misfit dislocations with a regular spacing of

$$\Lambda = a / \varepsilon \ . \tag{2.1}$$

In the upper wafer in regions near the dislocation cores, compressive strain exists in the lateral direction, whereas in regions between the dislocations the strain becomes tensile. The opposite is true in the lower wafer. This periodic strain field must also satisfy the mechanical equilibrium condition, i.e., at equilibrium there is no net force acting on any given volume element. With the additional boundary condition of diminishing strain away from the interface, a solution can readily be found (by first considering the Airy stress function [19]) for the upper wafer, i.e.,

$$\sigma_{xx} = \sigma_{zz} = \sum_{m=1}^{\infty} A_m e^{-m\zeta} \cos m\xi \tag{2.2}$$

and

$$\sigma_{xz} = \sum_{m=1}^{\infty} A_m e^{-m\zeta} \sin m\xi , \tag{2.3}$$

12

where σ_{xx} and σ_{zz} are the normal stresses and σ_{xz} is the shear stress, and where

$$\xi \equiv \frac{2\pi x}{\Lambda} \tag{2.4a}$$

$$\varsigma \equiv \frac{2\pi z}{\Lambda} . \tag{2.4b}$$

The A_m's are the coefficients to be determined by matching to the atomic arrangement along the interface. The solution for the lower wafer is similar but with some opposite signs. A simplification of retaining only the fundamental term $m = 1$ will be considered first for an illustration of the principles.

For elastically isotropic materials, the strains ε_{xx}, ε_{zz}, and ε_{xz} can be straightforwardly related to the stresses through equations containing the shear modulus μ and the Poisson's ratio v. The coefficient A can then be determined by matching to the boundary condition at the interface. For regions in between the dislocations, such as that near the origin in Figure 2-4, a symmetry consideration places the strain at $\varepsilon/2$, i.e.,

$$\varepsilon_{xx}(0,0) = \varepsilon / 2 . \tag{2.5}$$

Note that correction will be needed for any deviation from the symmetry assumption of equal elastic constants in the two materials. By comparing Equation (2.5) with the strain/stress equations, we have

$$A = \varepsilon\mu . \tag{2.6}$$

Substitution of Equation (2.6) into these equations yields the strain field.

The atomic displacements can now be evaluated by integrating the strain/stress equations. The foregoing analysis can be straightforwardly extended to the more realistic three-dimensional case, yielding the atomic displacements u_x and u_y parallel to the plane of the interface and u_z perpendicular to the plane,

$$u_x = \frac{a}{4\pi} e^{-\varsigma} \sin\xi \tag{2.7}$$

$$u_y = \frac{a}{4\pi} e^{-\varsigma} \sin\eta \tag{2.8}$$

and

$$u_z = \frac{a}{4\pi} e^{-\varsigma} (\cos\xi + \cos\eta) , \tag{2.9}$$

with

$$\eta \equiv \frac{2\pi y}{\Lambda} \; . \tag{2.10}$$

Note that Equation (2.9) leads to a wavy interface, e.g., along the x direction at $z = 0$,

$$u_z = \frac{a}{4\pi} \cos \frac{2\pi x}{\Lambda} \; . \tag{2.11}$$

This is reflected in the drawing in Figure 2-4, but with an exaggeration by a factor of 2, so that the wavy feature can be more clearly seen. Also note that the amplitude of the wavy atomic displacement quickly decays in a short distance from the interface because of the exponential factor $e^{-2\pi z/\Lambda}$ in Equations (2.7)–(2.9).

While the present solution appears to be accurate for regions between the dislocations, the strain near the dislocation cores is probably significantly underestimated. More accurate solutions can be obtained by including the higher-order terms in the Fourier expansion, but would require more detailed knowledge of the atomic arrangement near the dislocation core. However, these higher-order terms would represent effects that are even more short-range or localized as can be seen in the exponential factors in Equations (2.2) and (2.3).

The rapidly diminishing strain a short distance from the interface implies a minimal disturbance to the bulk of the materials during the wafer-fusion process, despite the considerable strain introduced to the interface. This is consistent with the experimental observation of virtually no dislocation generation in the wafer-fused materials. This is also consistent with the good device performance and reliability obtained, which are virtually identical to those fabricated on the original lattice-matched substrate. Such a result is rather different from the heteroepitaxial growth of thick layers on lattice-mismatched substrates, in which the strain relaxation resulted in high densities of threading dislocations in the grown layers [17],[18]. Thus, the wafer-fusion process is a viable alternative for integration with lattice-mismatched substrates without material degradation. The highly localized strain further precludes any stress-induced long-range diffusion and therefore ensures a long-term stability and reliability of the materials and devices.

The present work may also provide insight to the electrical characteristics of the interface. In particular, the strong alternating compressive and tensile strains along the interface should result in considerable modification of the energy-band structures and may lead to interesting applications such as quantum wires and dots. Further work is also needed to investigate the fused interface of wafers of large lattice and orientational mismatches.

<div align="center">Z. L. Liau</div>

2.3   EFFECT OF BUFFER LAYER GROWTH ON GaSb EPILAYERS GROWN ON GaAs SUBSTRATES

Measurement of intrinsic electrical properties such as background concentration and mobility of GaSb epilayers are typically performed on epilayers grown on semi-insulating (SI) GaAs substrates, since equivalent SI GaSb substrates are not available. However, because the lattice mismatch between GaSb and GaAs is 7.8%, the electrical properties can be deleteriously affected by interfacial dislocations that propagate through the epilayer, as has been reported for InAs grown on GaAs substrates [20],[21]. For heteroepitaxial growth, a two-step growth technique, which consists of first depositing a nucleation layer at low temperature followed by growth at a higher temperature, is commonly used to minimize threading dislocations [22],[23]. Here, we compare the electrical and structural qualities of GaSb epilayers grown on GaAs substrates using either a single-step procedure or a two-step procedure that includes a low-temperature low-growth-rate GaSb buffer layer.

The GaSb epilayers were grown in a vertical rotating-disk organometallic vapor phase epitaxy reactor operated at 150 Torr. The source materials were triethylgallium (TEGa) and trimethylantimony (TMSb). The carrier gas was H_2 at a flow rate of 10 slpm. Two procedures were used for growth of GaSb epilayers on SI (100) GaAs substrates, oriented 2° toward [110]. In the single-step procedure, GaSb was deposited on the GaAs substrate at a constant growth temperature, which was varied in different runs between 550 and 640°C. The TEGa mole fraction was 3×10^{-4} while the TMSb mole fraction ranged from 3 to 5.4×10^{-4}, depending on the growth temperature [24]. For the two-step procedure, a 100-nm-thick GaSb buffer layer was first grown at 550°C with TEGa and TMSb mole fractions of 1 and 1.8×10^{-4}, respectively. These conditions resulted in a growth rate of 3 Å/s. Growth was then interrupted and the substrate was heated to the final growth temperature (550–640°C). After the temperature stabilized, the bulk GaSb epilayer was grown under similar conditions as described for the single-step procedure. Layers were typically 3–4 μm thick. The surface was examined using Nomarski contrast microscopy or atomic force microscopy. Double-crystal x-ray diffraction (DCXRD) was used for structural characterization, and carrier concentration and mobility were obtained from Hall measurements based on the van der Pauw method.

The surface morphology of all GaSb epilayers grown using the two-step procedure was mirror-like while those grown in a single step were mirror-like only when the growth temperature was below 600°C. Otherwise, the surface exhibited a slight haze. The surface morphology of GaSb grown at 640°C using the single- or two-step procedure is shown in Figure 2-5. A significant improvement in the flatness of the surface is observed when the two-step method is employed.

The structural quality of GaSb on GaAs was examined by evaluation of the full width at half-maximum (FWHM) of DCXRD from the (400) reflection (Figure 2-6). For GaSb grown at 550, 575, or 580°C, the FWHM is ~ 150–180 arc sec whether the single- or two-step procedure is used. This FWHM value is relatively constant with growth temperature for epilayers grown using the two-step procedure, which suggests that growth of the GaSb buffer layer results in two-dimensional growth. For layers grown using a single step, however, the FWHM increased when the growth temperature increased above 580°C, suggesting three-dimensional growth and propagation of threading dislocations through the epitaxial GaSb layer.

15

286465-7
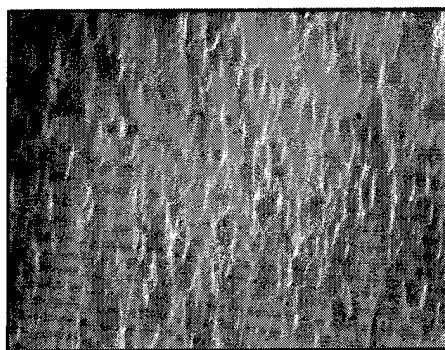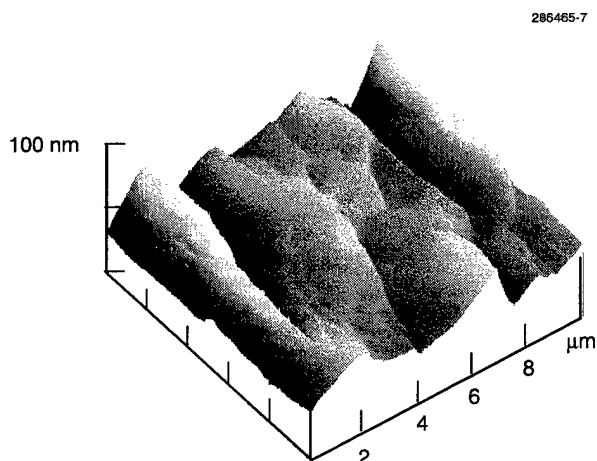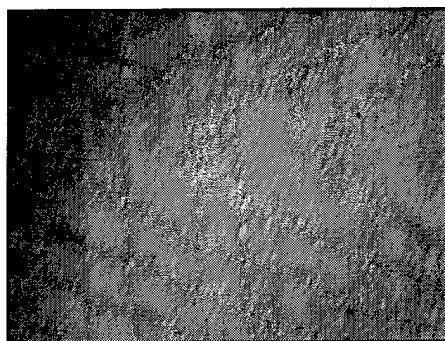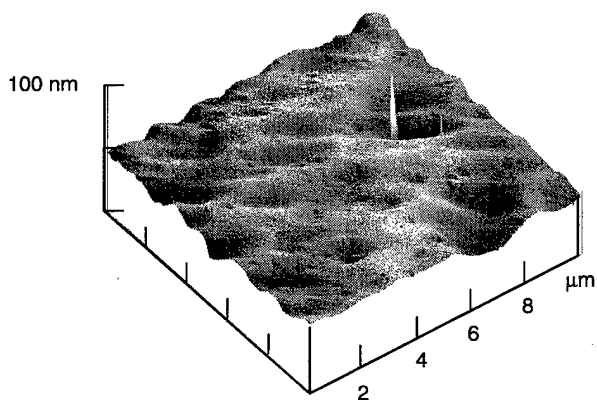
Figure 2-5. Nomarski contrast micrographs and atomic-force-microscopy images of GaSb epilayers on GaAs grown with the (a) single-step or (b) two-step procedure. The bulk GaSb epilayer was grown at 640°C.

16
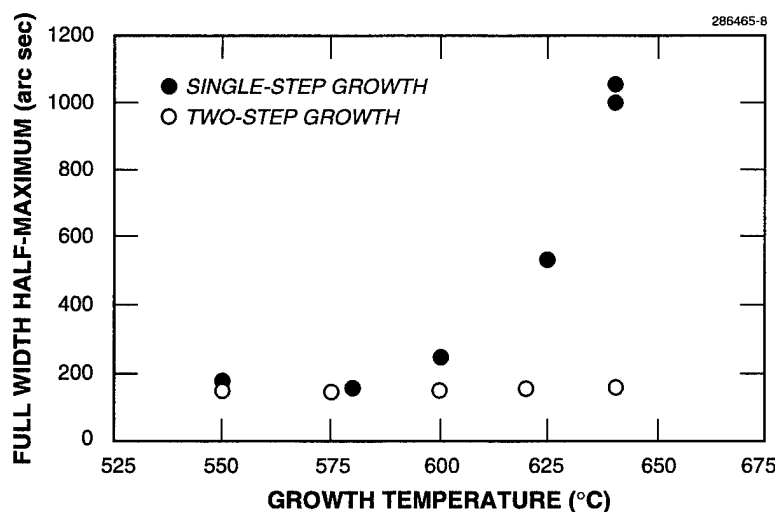
Figure 2-6. Full width at half-maximum of double-crystal x-ray diffraction of GaSb on GaAs as a function of growth temperature.

The electrical properties measured at 77 K of GaSb epilayers grown with the single- or two-step procedure are shown as a function of growth temperature in Figure 2-7. Nominally undoped epilayers are p-type, which has been attributed to (GaSb, VGa) native defects [25]. In general, the hole concentration (mobility) increases (decreases) with growth temperature whether the single- or two-step procedure is used. The electrical properties are comparable for layers grown at 550, 575, and 580°C, while improvements in the electrical characteristics are most notable for layers grown above 575°C, consistent with DCXRD results. The best electrical properties were measured for GaSb grown at 550°C using the single-step procedure with μ_{77} = 5800 cm^2/V s and a corresponding hole concentration p_{77} = 2.9 × 10^{15}cm^{-3}. These values are comparable to the best values reported for GaSb grown by molecular beam epitaxy and organometallic vapor phase epitaxy [26],[27].

C. A. Wang   D. R. Calawa

R. J. Poillucci   L. M. Eriksen

17

HOLE CONCENTRATION AT 77 K (cm^{-3})

286465-9

● SINGLE-STEP GROWTH
○ TWO-STEP GROWTH

1.5×10^{16}
1.3×10^{16}
1.1×10^{16}
9×10^{15}
7×10^{15}
5×10^{15}
3×10^{15}
1×10^{15}

525   550   575   600   625   650   675

GROWTH TEMPERATURE (°C)

(a)

HOLE MOBILITY AT 77 K (cm^2/V s)

7000
6000
5000
4000
3000
2000

● SINGLE-STEP GROWTH
○ TWO-STEP GROWTH

525   550   575   600   625   650   675

GROWTH TEMPERATURE (°C)

(b)
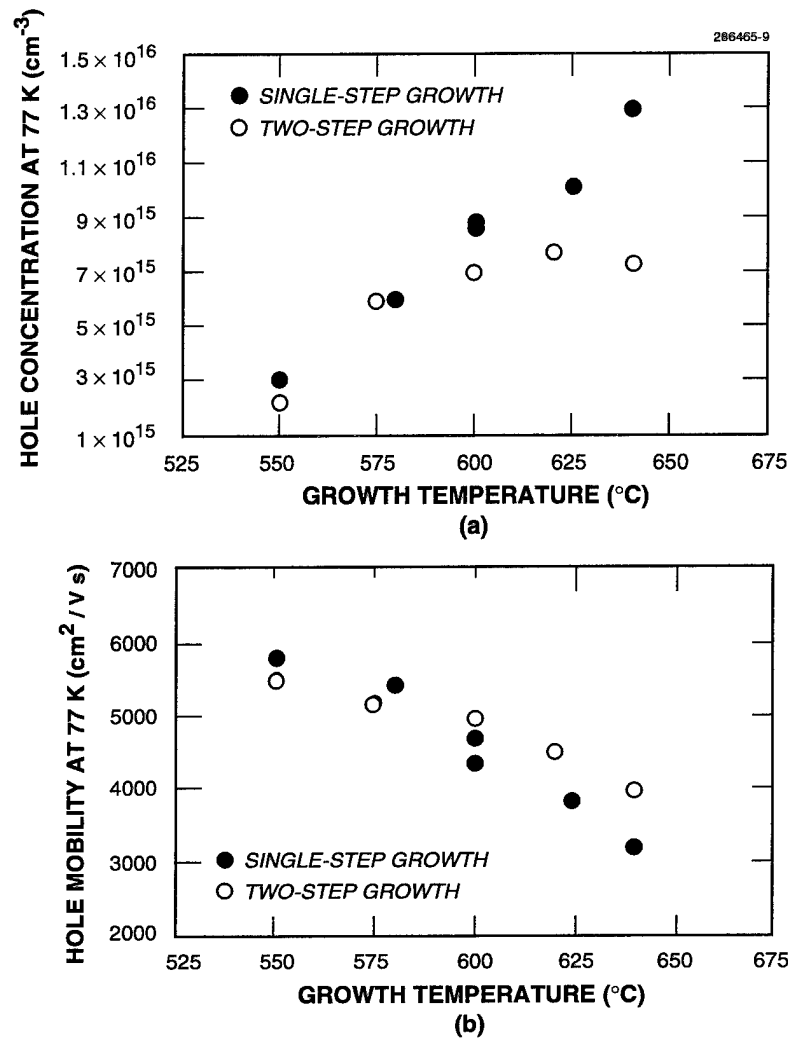
Figure 2-7. (a) Hole concentration and (b) hole mobility at 77 K as a function of growth temperature for GaSb grown using the single-step or two-step procedure.

2.4 HIGH CW POWER (> 200 mW/FACET) AT 3.4 μm FROM InAsSb/InAlAsSb STRAINED-QUANTUM-WELL DIODE LASERS

High-performance semiconductor diode lasers emitting in the mid-infrared (mid-IR) spectrum of 2–5 μm are very desirable for a variety of applications that exploit the characteristics of this spectral range, including strong molecular absorption lines and important atmospheric transmission windows. Single-frequency mid-IR diode lasers are ideally suited for highly sensitive detection of trace gases for

such applications as pollution or toxic gas monitoring and industrial process control. In addition, high-power mid-IR lasers emitting in the atmospheric transmission windows can be very useful for laser radars, infrared countermeasures, and target designation/illumination.

Although GaInAsSb/AlGaAsSb strained-quantum-well (QW) diode lasers have exhibited very good room-temperature performance in the 2-μm region [28],[29], diode lasers emitting beyond 3 μm had relatively poor performance. Recently, however, significant progress has been made at ~ 3.4 μm using InAsSb/InAlAsSb strained QW lasers, which exhibited pulsed operation up to 225 K and CW up to 175 K [30]. Here, we report high-power operation of these lasers, with power up to 215 mW/facet at 80 K. To our knowledge, this is the highest power obtained for any semiconductor laser emitting beyond 2.2 μm.

The QW laser structure was grown on a 2-in.-diam epi-ready (100) n-InAs substrate in a solid-source molecular beam epitaxy system with a valved As_2 cracking source. Details of the growth procedure were reported previously [31]. The laser has the following structure: 0.5-μm-thick n^+-InAs buffer, 2-μm-thick n-AlAs$_{0.16}$Sb$_{0.84}$ cladding, multiple-QW active region consisting of ten 15-nm-thick InAs$_{0.935}$Sb$_{0.065}$ wells and eleven 30-nm-thick In$_{0.85}$Al$_{0.15}$As$_{0.9}$Sb$_{0.1}$ barriers, 0.1-μm-thick p-AlAs$_{0.16}$Sb$_{0.84}$ and 1.9-μm-thick p-Al$_{0.1}$Ga$_{0.9}$As$_{0.14}$Sb$_{0.86}$ cladding, and 10-nm-thick p^+-GaSb cap layer. The active region is designed to be strain balanced to avoid dislocation formation. No graded layers were incorporated in the structure. The surface observed by Nomarski interference microscopy is mirror smooth.

Broad-stripe lasers 100 and 250 μm wide were fabricated by using SiO_2 patterning. For both n and p contacts, nonalloyed Ti/Pt/Au was used. Lasers were mounted junction-side up on Cu heatsinks using In, and loaded into a dewar for low-temperature measurements. Figure 2-8 shows the current vs voltage curves for a 100 × 1000-μm device at 300, 200, and 100 K. The turn-on voltage increases from 0.5 V at 300 K to 1.6 V at 100 K. The high turn-on voltage is caused by large barriers at the substrate/n-cladding as well as n-cladding/barrier interfaces, which are due to large conduction-band offsets. These high barriers also increase the series resistance.
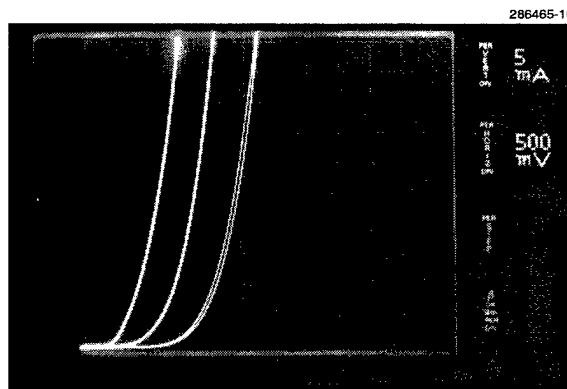
Figure 2-8. Forward current vs voltage curves of a 100 × 1000-μm device at 300, 200, and 100 K (from left to right).

Figure 2-9 shows the pulsed threshold current density as a function of temperature for a 1000-μm-long device. At 80 K, the value of J_{th} is 44 A/cm^2. At this temperature, the contribution of Auger recombination to J_{th} may be small. The slope of the curve in Figure 2-9 is characterized by a temperature T_0 which, between 80 and 100 K, is larger than 50 K but gradually decreases at higher temperatures, reaching a value of 25 K at 200 K. The maximum pulsed operating temperature is 220 K.

For CW measurements, devices were mounted junction-side down on heatsinks, and loaded into a low-temperature dewar. Output power was measured using a thermopile detector. For cavity lengths of 500, 1000, and 1500 μm, initial differential quantum efficiencies at 80 K are 45, 35, and 28%, respectively. From these values, the internal quantum efficiency and internal loss coefficient are estimated to be 63% and 9 cm^{-1}, respectively. The differential quantum efficiency remains more or less constant up to 140 K, and then decreases gradually. Even at 200 K, the efficiency is approximately one third of the low-temperature values. In contrast, the efficiency of double-heterostructure lasers emitting in the same wavelength range decreased much more rapidly with temperature [32].
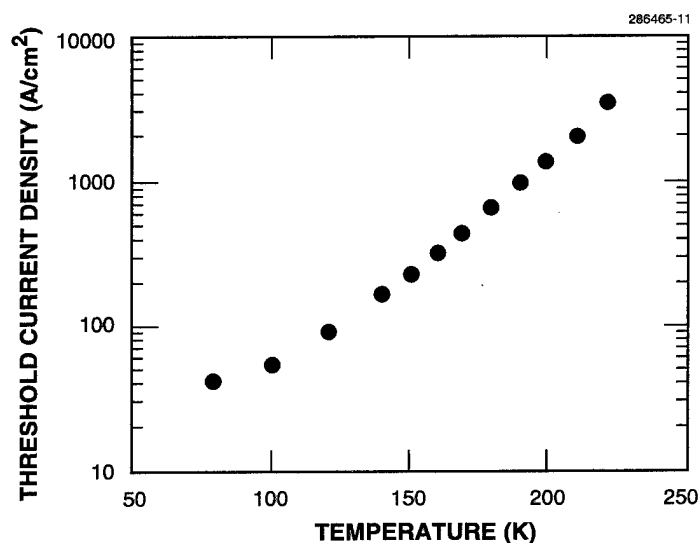
Figure 2-9. Pulsed threshold current density vs temperature of 250 × 1000-μm device.

20
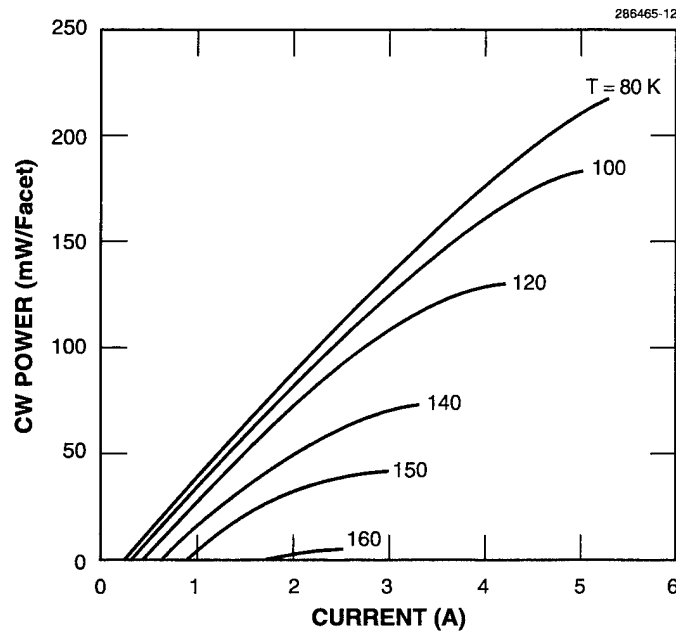
Figure 2-10. CW power vs current of 250 × 1000-μm device at several temperatures.

Figure 2-10 shows the output power vs current of a 1500-μm-long device at several temperatures. At 80 K, the threshold current is 150 mA, and the maximum power is 215 mW/facet, limited by junction heating. The maximum output power decreases with temperature, and at 150 K it is ~ 35 mW/facet. The operating voltage for the maximum power is ~ 4 V at 80 K, which is more than 10 times larger than the photon energy. Substantially higher output power is expected if the operating voltage can be reduced by incorporating graded interfaces in the structure.

H. K. Choi   M. J. Manfra
G. W. Turner   W. L. McGilvary

21

REFERENCES

1. L. F. Tiemeijer, *Appl. Phys. Lett.* **59**, 499 (1991).

2. M. C. Tatham, G. Sherlock, and L. D. Westbrook, *IEEE Photon. Technol. Lett.* **5**, 1303 (1993).

3. S. Murata, A. Tomita, J. Shimizu, and A. Suzuki, *IEEE Photon. Technol. Lett.* **3**, 1021 (1991).

4. J. Zhou, N. Park, J. W. Dawson, K. J. Vahala, M. A. Newkirk, and B. I. Miller, *Appl. Phys. Lett.* **62**, 2301 (1993).

5. K. Inoue, T. Hasegawa, K. Oda, and H. Toba, *Electron. Lett.* **29**, 1708 (1993).

6. T. Hasegawa, K. Inoue, and K. Oda, *IEEE Photon. Technol. Lett.* **5**, 947 (1993).

7. H. Q. Le and S. DiCecca, *Opt. Lett.* **4**, 901 (1991).

8. H. Q. Le and S. DiCecca, *IEEE Photon. Technol. Lett.* **4**, 878 (1992).

9. H. Q. Le, W. D. Goodhue, and K. Rauschenbach, *Opt. Lett.* **15**, 1126 (1990).

10. A. M. Darwish, G. Lenz, E. P. Ippen, H. Q. Le, J. P. Donnelly, S. H. Groves, and E. A. Swanson, *Quantum Electronics Conference*, Vol. 16, 1995 OSA Technical Digest Series (Optical Society of America, Washington, D.C., 1995), p. 229.

11. Z. L. Liau and D. E. Mull, *Appl. Phys. Lett.* **56**, 737 (1990).

12. Y. H. Lo, R. Bhat, D. M. Hwang, M. A. Koza, and T. P. Lee, *Appl. Phys. Lett.* **58**, 1961 (1991).

13. D. I. Babic, J. J. Dudley, K. Streubel, R. P. Mirin, J. E. Bowers, and E. L. Hu, *Appl. Phys. Lett.* **66**, 1030 (1995).

14. L. Gordon, G. L. Woods, R. C. Eckardt, R. R. Route, R. S. Feigelson, M. M. Fejer, and R. L. Byer, *Electron. Lett.* **29**, 1942 (1993).

15. F. A. Kish, F. M. Steranka, D. C. DeFevere, D. A. Vanderwater, K. G. Park, C. P. Kuo, T. D. Osentowski, M. J. Peanasky, J. G. Yu, R. M. Fletcher, D. A. Steigerwald, M. G. Craford, and V. M. Robbins, *Appl. Phys. Lett.* **64**, 2839 (1994).

16. Y. Okuno, K. Uomi, M. Aoki, T. Taniwatari, M. Suzuki, and M. Kondow, *Appl. Phys. Lett.* **66**, 451 (1995).

17. S. F. Fang, K. Adomi, S. Iyer, H. Morkoç, H. Zabel, C. Choi, and N. Otsuka, *J. Appl. Phys.* **68**, R31 (1990).

18. H. K. Choi, J. W. Lee, J. P. Salerno, M. K. Connors, B. Y. Tsaur, and J. C. C. Fan, *Appl. Phys. Lett.* **52**, 1114 (1988).

19. See, for example, J. P. Hirth and J. Lothe, *Theory of Dislocations* (McGraw-Hill, New York, 1968), p. 43.

20. B. J. Baliga and S. K. Ghandhi, *J. Electrochem. Soc.* **121**, 1646 (1974).

21. M. Yano, M. Nogami, Y. Matsushima, and M. Kimata, *Jpn. J. Appl. Phys.* **16**, 2131 (1977).

22. M. Akiyama, Y. Kawarada, and K. Kaminishi, *Jpn. J. Appl. Phys.* **23**, L843 (1984).

23. T. Ueda, S. Onozawa, M. Akiyama, and M. Sakuta, *J. Cryst. Growth* **93**, 517 (1988).

24. C. A. Wang, S. Salim, K. F. Jensen, and A. C. Jones, to be published in *J. Cryst. Growth.*

25. Y. J. Van der Meulen, *J. Phys. Chem. Solids* **28**, 25 (1967).

26. A. Baraldi, C. Ghezzi, R. Magnanini, A. Parisini, L. Tarricone, A. Bosacchi, S. Franchi, V. Avanzini, and P. Allegri, *Mater. Sci. Eng.* **B28**, 174 (1994).

27. F. Royo, A. Giani, F. Pascal-Delannoy, L. Gouskov, J. P. Malzac, and J. Camassel, *Mater. Sci. Eng.* **B28**, 169 (1994).

28. H. K. Choi, G. W. Turner, and S. J. Eglash, *IEEE Photon. Technol. Lett.* **6**, 7 (1994).

29. H. Lee, P. K. York, R. J. Menna, R. U. Martinelli, D. Z. Garbuzov, S. Y. Naryan, and J. C. Connolly, *Appl. Phys. Lett.* **66**, 1942 (1995).

30. H. K. Choi, G. W. Turner, M. J. Manfra, and M. K. Connors, *Appl. Phys. Lett.* **68**, 2936 (1996).

31. G. W. Turner, H. K. Choi, and H. Q. Le, *J. Vac. Sci Technol. B* **13**, 699 (1995).

32. H. Q. Le, G. W. Turner, H. K. Choi, J. R. Ochoa, A. Sanchez, J. M. Arias, M. Zandian, R. R. Zucca, and Y.-Z. Liu, *Proc. SPIE* **2382**, 262 (1995).

3. SUBMICROMETER TECHNOLOGY

3.1 LASER-INDUCED MICROCHEMICAL ETCHING OF SILICON FOR TERAHERTZ-BASED WAVEGUIDE COMPONENTS

Waveguide components are critical elements in the design of low-noise, high-efficiency heterodyne receivers and local oscillators. However, at frequencies > 500 GHz, these components become exceedingly difficult to fabricate using conventional techniques. Feature sizes < 200 μm (8 mils) must be machined to tolerances within 5 μm (0.2 mil) over the entire device. Even when aggressive macromachining is employed in conjunction with electrodischarge or die-sink milling, the fabrication of fine-scale features is a time-consuming process. For example, waveguide structures fabricated at 490 GHz may take several weeks to fabricate and require significant operator intervention. Clearly, a more rapid and flexible technique for prototyping higher-frequency devices at even more demanding feature sizes and tolerances is required to extend communication and spectroscopic-based applications to the terahertz regime.

In a previous report [1], we summarized the process physics for a laser-based direct-write technique for fabricating three-dimensional structures in silicon. This technology is well suited for the waveguide application because it has demonstrated micrometer tolerances at high removal rates. The process makes use of an argon-ion laser beam to locally melt a portion of the silicon substrate. In the presence of chlorine, volatile silicon chlorides are formed that readily diffuse from the surface, limiting redeposition. The use of chemical activation also reduces the energy requirement for removal compared to purely thermal or mechanical techniques, minimizing the potential for damage. The process is extremely rapid, allowing removal rates ranging from ~ 10^4–10^5 μm^3/s for 1–10-μm resolutions, respectively. Through rapid scanning of the laser beam, etch depths can be limited to submicrometer shavings. Below, we report on our initial work in fabricating a portion of an 810-GHz and 2.5-THz circular-to-rectangular mode-matching waveguide designed by Prof. C. Walker of the Steward Observatory at the University of Arizona. We have also begun to investigate replication techniques to produce high-performance phased-array receivers based on the laser-etched prototypes.

The proposed feedhorn structure couples radiant energy through a ribbed feedhorn section into a rectangular waveguide that interfaces with an integrated detector. In the initial prototyping of the 810-GHz waveguide structure, an ~ 8-μm-diam laser-induced reaction zone is swept across the surface in 2-μm increments removing 1-μm shavings per pass at a rate of 10^5 μm^3/s. Higher scanning velocities can be used to increase depth resolution. Improved lateral resolutions, if necessary, are possible over critical dimensions through power modulation of the laser beam. Figure 3-1 shows a portion of the waveguide structure etched in 1 h (a duplicate mating piece must be fabricated). A larger feedhorn section for improved collection efficiency is shown in Figure 3-2.

286465-13
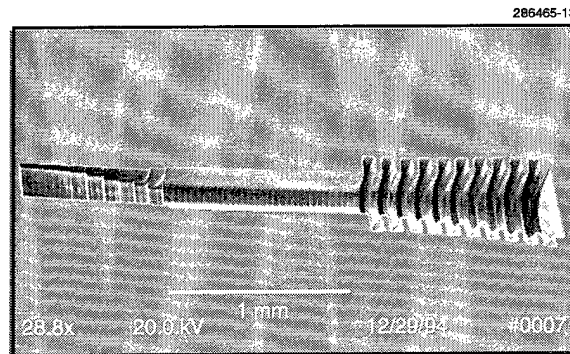
(a)
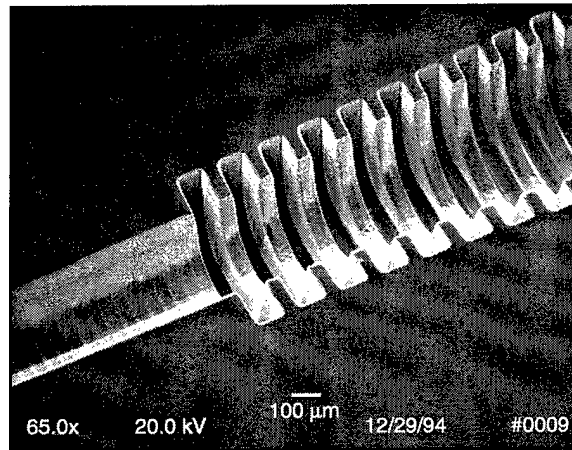
(b)

Figure 3-1. (a) *Scanning electron micrograph (SEM) of portion of 810-GHz waveguide structure, and* (b) *SEM close-up of ridges on the feedhorn portion of the structure. The structure was etched using 4.3 W of laser power focused into a 6-μm spot in 200 Torr of chlorine gas. The laser beam was scanned at 5 cm/s and incrementally moved 2 μm between line scans. Under these conditions, nominally 1-μm shavings are removed per pass of the laser over the surface.*

26
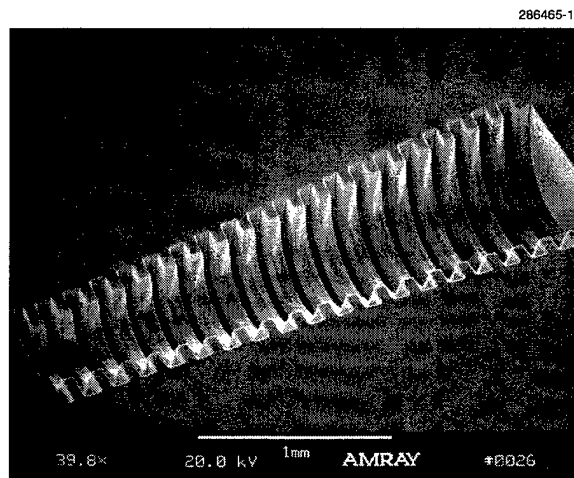
Figure 3-2. SEM of a 20-ridged feedhorn section of the 810-GHz waveguide. The same processing conditions described in Figure 3-1(a) were used. This extended portion of the feedhorn required 2.5 h to fabricate.

Further work is required to metallize the surfaces and package the device with the detector before testing. However, this technology already has the potential to produce waveguide components that are difficult or impossible to manufacture using conventional techniques. Higher-frequency waveguide components can be fabricated in even less time since volumetric removal rates scale linearly with melt-zone diameter [1], or resolution, while the total volume of the device scales cubically with length scale. For instance, a similar 1.78-THz waveguide at 4-μm resolution can be etched in one fourth the time of the 810-GHz version. In addition, fabricating the structures in silicon may allow electronic detectors to be integrated directly at the output stage of a device.

We are also currently working on a polymer-based replication process [2] to produce high-performance, low-cost focal plane arrays at terahertz frequencies. This molding process has shown extremely high fidelity in reproducing features down to submicrometer detail. A negative of the silicon-etched master is first made by casting polydimethylsiloxane (PDMS) over the etched surface, which has been first fluorinated with tridecafluoroctaltrichlorosilane (TDTS). Because of the high elastomeric constant and low interfacial free energy between PDMS and the surface, it can be readily pulled apart from the silicon master. A low-viscosity polymer precursor, such as ultraviolet-curable epoxy, polyurethane, or polymethylmethacrylate, is then flowed over the elastomer negative, filling the structure through capillary action. After curing, the elastomer is pulled from the epoxy replica for further reuse. A portion of a replicated 2.5-THz waveguide structure, in 5-min ultraviolet-cured epoxy, is shown in Figure 3-3.

27
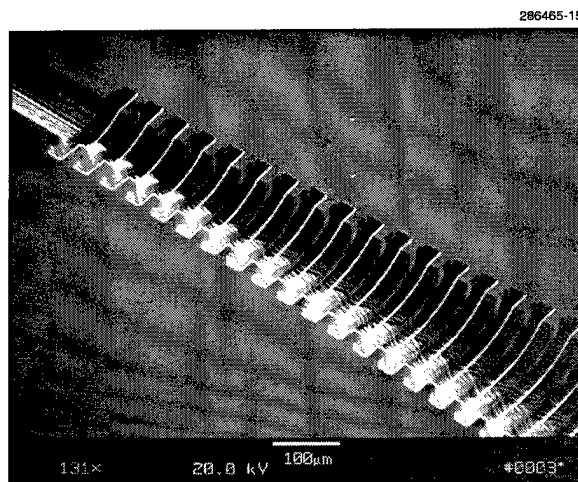
Figure 3-3. SEM micrograph of replicated version of 2.5-THz waveguide structure. The original structure was etched using 3 W of laser power focused into a 4-μm spot in 200 Torr of chlorine gas. The laser beam was scanned at 2 cm/s and incrementally moved 2 μm between line scans removing 1-μm shavings per pass of the laser over the surface.

From these initial proof-of-concept results, we believe laser-induced microchemical etching of silicon in conjunction with replication techniques is a promising technology for extending spectroscopy and communication-based applications to the terahertz regime.

T. M. Bloomstein   M. B. Stern
S. Palmacci   J. E. Curtin
C. Walker*

3.2 OPTICAL SAMPLING FOR ANALOG-TO-DIGITAL CONVERTERS

Optical sampling of an electrical signal has many potential advantages for analog-to-digital (A/D stability) converters. The timing stability of pulses generated by a mode-locked laser is extraordinary. This offers the prospect of precise, high-speed sampling well beyond what can be achieved with electronic-switch-based sampling. Electrooptic modulators provide a wide bandwidth method of imposing an electrical signal on an optical pulse train. The difficulty with such modulators is their limited dynamic range due to the inherent nonlinearity of the interferometer on which the modulator is based. Signal processing hardware has advanced sufficiently in recent years to permit real-time linearization of these modulators. This report describes the performance of an initial realization of such a system, an A/D converter based on optical sampling and linearization techniques, as shown in Figure 3-4. This architecture provides substantial system benefits. The optical isolation of the input signal from other noise sources

*Author not at Lincoln Laboratory.

28

makes realization of the potential precision of this system practical. The optical signals can be carried on fibers, allowing remote sensing with high precision and wide bandwidth. Finally, because light simply doesn't interact with the electrical signal applied to the modulator, this optical sampling technique can be used as an extremely linear, wideband mixer.

Recently, harmonically mode-locked, erbium fiber lasers have become commercially available. These lasers have pulse repetition rates ranging from hundreds of megahertz to tens of gigahertz. The timing jitter of the output pulses can be < 50 fs. The pulse width can be controlled independently of the repetition rate with a simple optical filter over a range 1–100 ps. These pulses can be amplified to average power levels of several watts with compact and efficient erbium fiber amplifiers. In comparison, the best electrical sampler has a timing jitter of 250 fs, while commercial devices operate in the picosecond regime.
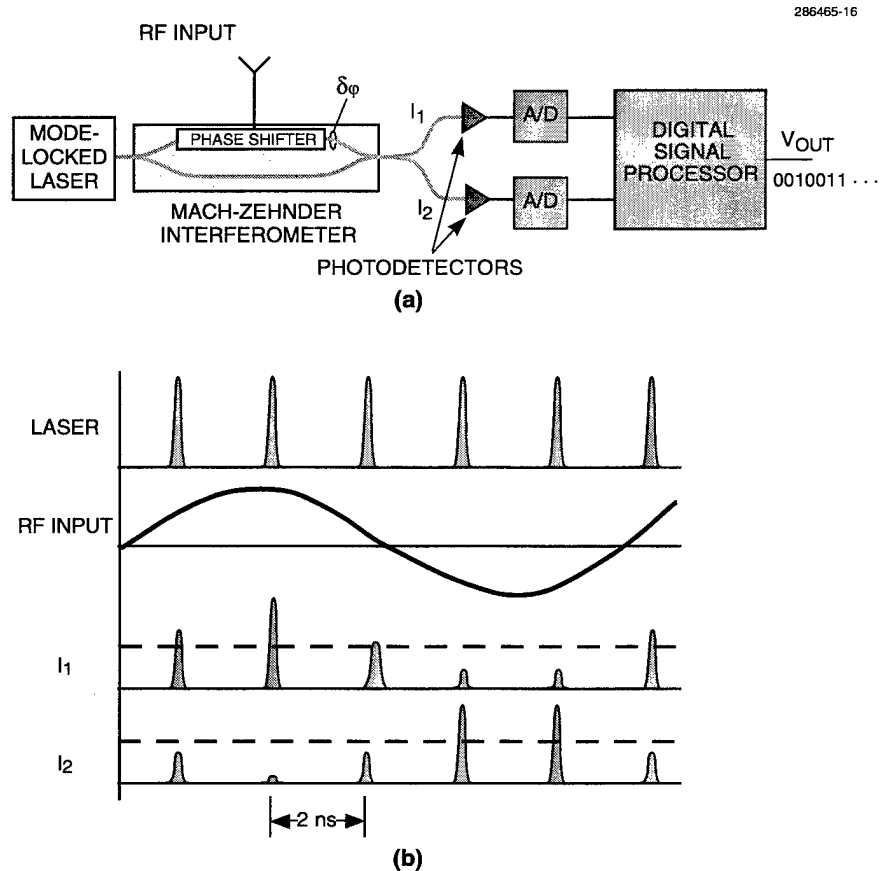
Figure 3-4. (a) *Schematic illustration of analog-to-digital converter system that uses optical sampling. The mode-locked laser generates a train of short, precisely timed optical pulses that enter the interferometer and sample the RF input.* (b) *Representative system waveforms.*

29

Most wideband electrooptic modulators are simple Mach-Zehnder interferometers. The electrical signal induces a slight change in the index of refraction of one leg of the interferometer relative to the other leg. The result is a phase shift in the optical signals, which are then coherently summed at the output of the interferometer. The output of the interferometer exhibits classic fringes with a sinusoidal dependence on the electrically induced phase shift. The sinusoidal dependence of the output intensity is the fundamental source of the nonlinearity that limits the dynamic range of the modulator. However, the phase shift is linearly related to the input voltage, making it possible to restore linearity by processing the signals as described below.

Figure 3-5 illustrates the mapping of signals through the various components of the system. The phase shift in the modulator is calculated from the intensities of the two output legs as follows:

$$\delta\varphi = \arcsin\left(\frac{I1 - I2}{I1 + I2}\right) .$$ (3.1)

This optical transform has several interesting properties. First, notice that the phase is independent of the total intensity since the intensity difference (the numerator) is normalized to the total intensity. Physically, the interferometer conserves photons, and thus all light entering the device leaves through one of the two output ports. Next, notice that the Taylor expansion about zero for the arcsine function,

$$\arcsin(z) = z + \frac{1}{2 \cdot 3} z^3 + \frac{3}{2 \cdot 4 \cdot 5} z^5 + \frac{3 \cdot 5}{2 \cdot 4 \cdot 6 \cdot 7} z^7 \dots ,$$ (3.2)

has no even powers of z. The strongest deviation from linearity is seen to be the $z^3/6$ term. If the input voltage is constrained to be small, then the corrections required will be small, but *not* ignorable. If we seek 90 dB of dynamic range for a signal corresponding to 0.1 radian (about −10 dBm), we will have to correct to the seventh-order term. The only difficulty this presents is that we must carry the seventh harmonic from the photodetector to the digitizer. This illustrates a trade between detector bandwidth and peak signal that this technique imposes on the system architecture.
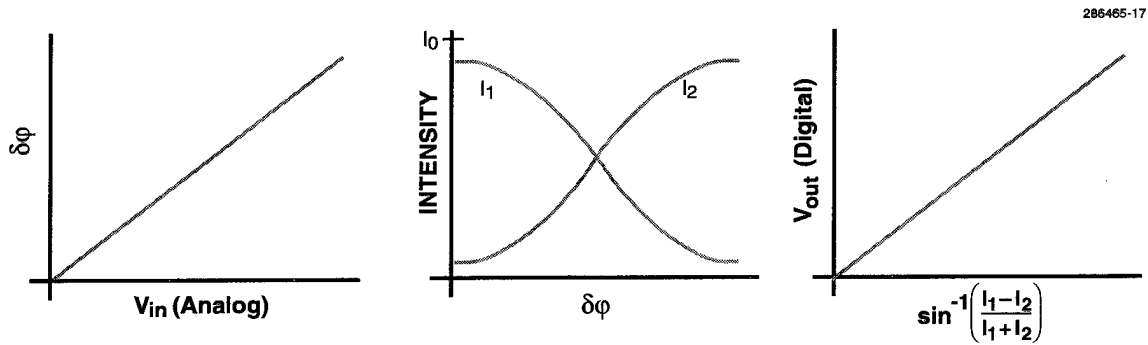
Figure 3-5. Transfer characteristics for the system components shown in Figure 3-4: (a) Mach-Zehnder interferometer phase characteristic, (b) interferometer intensity characteristic, and (c) linearization of the output.

For most practical systems the dynamic range will be limited by the digitizer, and the peak signal will be limited by the desired sensitivity. Typically, only the third-order correction term needs to be kept to maintain 90 dB of linearity. Thus, only the third harmonic is required to pass through the photodetectors and amplifiers. Note that this constraint does not apply to the modulator bandwidth. The modulator is a linear device (in phase), and it is only the coherent summing of the two arms of the interferometer that causes the intensity nonlinearity.

To test this approach to optical sampling, a narrowband UHF sampler was constructed, as shown in Figure 3-6. By setting the input frequency close to the laser pulse repetition frequency, the input signal is deliberately aliased into the 0.5-MHz digitizer bandwidth. The laser used was an ordinary 1.3-μm semiconductor laser that was gain switched by pulsing the input with a resonantly coupled step-recovery diode comb generator. This produced a 500-MHz train of 130-ps pulses with an estimated jitter time of 1 ps. The average power of this optical pulse train was about 400 μW. A standard commercial lumped-element electrooptic modulator was used. This modulator had only 1.5 GHz of bandwidth. A two-tone generator was used to generate a pair of tones separated by 8.683 kHz at 499.902 MHz.

The data were digitized to 12 bits of precision and read into a computer. The computer applied the transform described above to determine the modulator phase, and calculated the voltage applied to the modulator and the resulting power spectrum. Figure 3-7 shows the result. The third-order intermodulation distortion products are not visible against the noise floor 84 dB below the –10-dBm carrier. This demonstrates that the third-order intermodulation distortion is less than –90 dB. The spur-free dynamic range is shown to the 78 dB, limited by the digitizer used.

286465-18
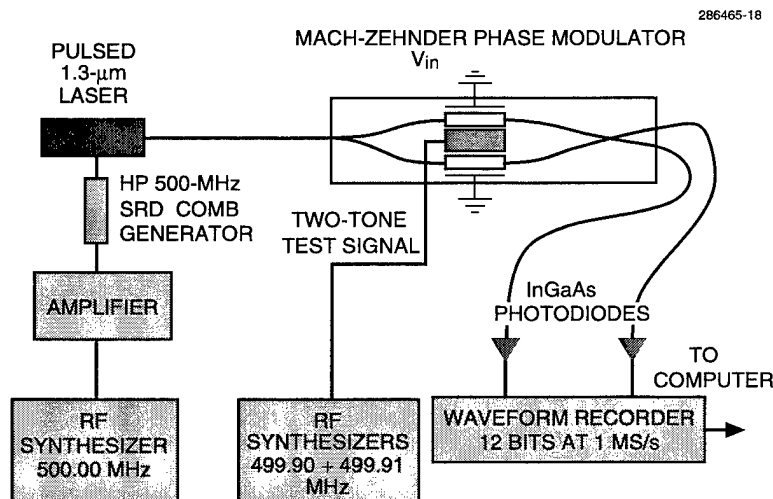
Figure 3-6. Experimental setup used to test the optical sampling technique. The semiconductor laser is gain switched with an RF-driven step-recovery diode (SRD) comb generator to produce a train of 130-ps pulses at 500 MHz. These pulses sample the two-tone test signal. MS is megasample.

31

Similar tests were performed with input signals at 999.897 MHz, leaving the laser pulse repetition frequency at 500 MHz. Although the harmonics of this signal lie far outside the bandwidth of the modulator, the results were essentially identical to the previous tests. This illustrates that the input signals and modulator bandwidth do not have to carry any of the higher harmonics necessary to remove the interferometer nonlinearity. It was necessary to maintain the bandwidth into the A/D at several times the measurement bandwidth. With our 100-kHz offset frequency tones, we needed an accurate third and fifth harmonic. We found the digitizer's first-order filter 3-dB point of 2.5 MHz was barely adequate.

These tests demonstrated that optical sampling can be performed with outstanding linearity. The narrowband tests alleviate the requirement for extremely precise pulse timing as the detectors and amplifiers average many pulses per digitizer measurement. This in turn reduces the effect of high-frequency pulse jitter. Such narrowband systems can exploit the linearity and short pulse width of optical sampling to greatly simplify the receiver architecture. Most radars and many communication systems fall into this class of narrowband digital receivers.
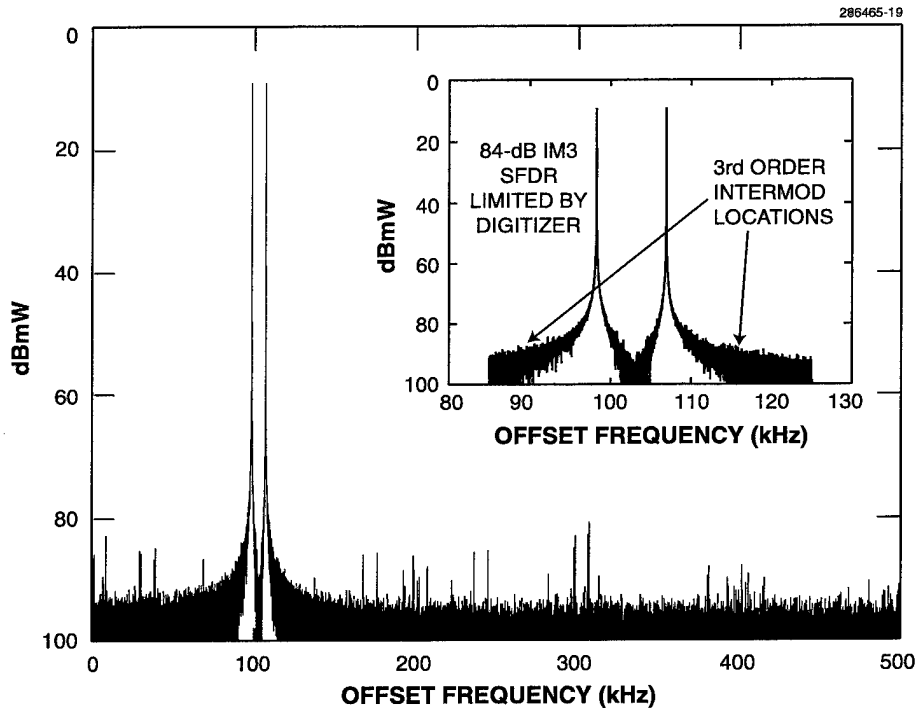
Figure 3-7. Results for two-tone spur-free dynamic range (SFDR) and (inset) third-order intermodulation test. The intermodulation products are at least 84 dB below the –10-dBm input. Since each of the two tones is –10 dBm, the resulting intermodulation-free dynamic range is 90 dB. The largest spur for the entire 500-kHz bandwidth is 78 dB below the –10-dBm input. Both these measures are limited by the performance of the digitizer used.
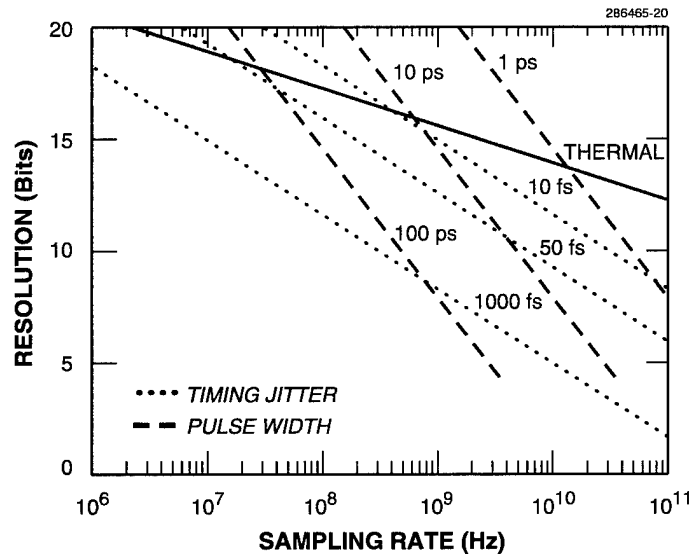
Figure 3-8. Illustration of fundamental limits imposed on wideband samplers by three processes: (1) the finite pulse width low-pass filters the data unless the pulse width is kept short compared to the period of the highest frequency of interest; (2) the timing jitter of the sample pulse causes errors for any time-varying signal, limiting the performance of all high-speed digitizers; and (3) for a 1-V peak input signal, thermal noise will limit accuracy, especially at low data rates.

Some applications demand wideband sampling of the data. That is, sampling of the input signal must occur at twice the highest frequency of interest. This retains all the information present in the signal. The timing precision and linearity possible with optical sampling using existing commercial components permit gigasample-per-second digitizers with 12 bits of precision. Figure 3-8 plots the three fundamental constraints limiting the accuracy of wideband digitizers: pulse width, timing jitter, and thermal noise. While present electrical samplers are approaching fundamental physical limits with 100-ps pulse widths and 250-fs jitter times, optical sampling can easily operate with pulse widths below 10 ps and with timing jitters < 50 fs. At some point, the power required to avoid shot-noise limits will cause optical damage, and thus optical power will eventually limit sampling accuracy.

J. C. Twichell
R. Helkey

33

REFERENCES

1. Solid State Research Report, Lincoln Laboratory, MIT, 1996:2, p. 13.

2. E. Kim, Y. Xia, and G. M. Whitesides, *Nature* **376**, 581 (1985).

4. HIGH SPEED ELECTRONICS

4.1 THE MICROSHUTTER: A NEW DISPLAY DEVICE

A new device has been discovered that has a large potential impact on electronic displays. The device is a light valve, which we are calling a microshutter, and has a fundamentally simple electromechanical structure that is easy to make and has been shown to be highly reliable. It also has some fundamental efficiencies that significantly exceed those of any other display device, and it is our belief that displays made with microshutters will be far lass expensive to produce.

Cross-sectional diagrams of the microshutter device in the open and closed positions are shown in Figure 4-1, along with the corresponding scanning electron microscope views of an actual device. The moving part of the microshutter is a very thin metal membrane that is made as a thin film in such a way that it can later be made to coil up; the device can be thought of as a spring attached to the substrate at one end. The substrate is glass with transparent conductor and insulator coatings. A voltage of 20 V applied between the transparent conductor and the membrane creates an electric field and therefore a force between the transparent conductor and the spring that exceeds the spring force. Once the 20-V rollout threshold is exceeded for this particular geometry, the entire length of the spring rolls out without stopping until only the very tip is still slightly off the surface. If the voltage is reduced below the 12-V roll up threshold the entire spring coils up. At voltages between 12 and 20 V the shutter can be either rolled up or rolled out, a feature which can be used to great advantage as a memory effect in a display. Part of an array of the devices is shown in Figure 4-2.

For flat panel displays the microshutter has advantages over the liquid crystal display (LCD) that is commonly used in digital watches, calculators, computers, and recently in small televisions. The liquid crystal device is basically a light valve or shutter that opens and closes under the action of an alternating electric field. It is most often used as a passive device either under ambient light in the reflection mode or backlit, or both. In spite of their wide use, LCDs have some inherent disadvantages, such as low speed, temperature sensitivity, and the requirement for polarizers (this restricts the viewing angle and limits the light throughput). In addition, LCDs do not have memory so that when they are used in an x-y scanning array, such as in television applications, an additional switch and storage element must be provided at each pixel. This usually means that a transistor and capacitor must be fabricated at each pixel, greatly adding to the cost of the display.

The microshutter does not use polarizers and therefore can potentially provide a display having a very high brightness because a large fraction of the light incident on the back of the device is transmitted when the device is full on. The brightness is predicted to be a factor of 3–5 times higher than the active matrix LCDs for the same backlight. The response time of the shutters is 40 μs, and our current devices have been operated successfully over the temperature range –40 to 170°C, which is considerably better than can be achieved with active matrix liquid displays. The resolution of our displays is currently 250 dots per inch with 500 easily achievable.
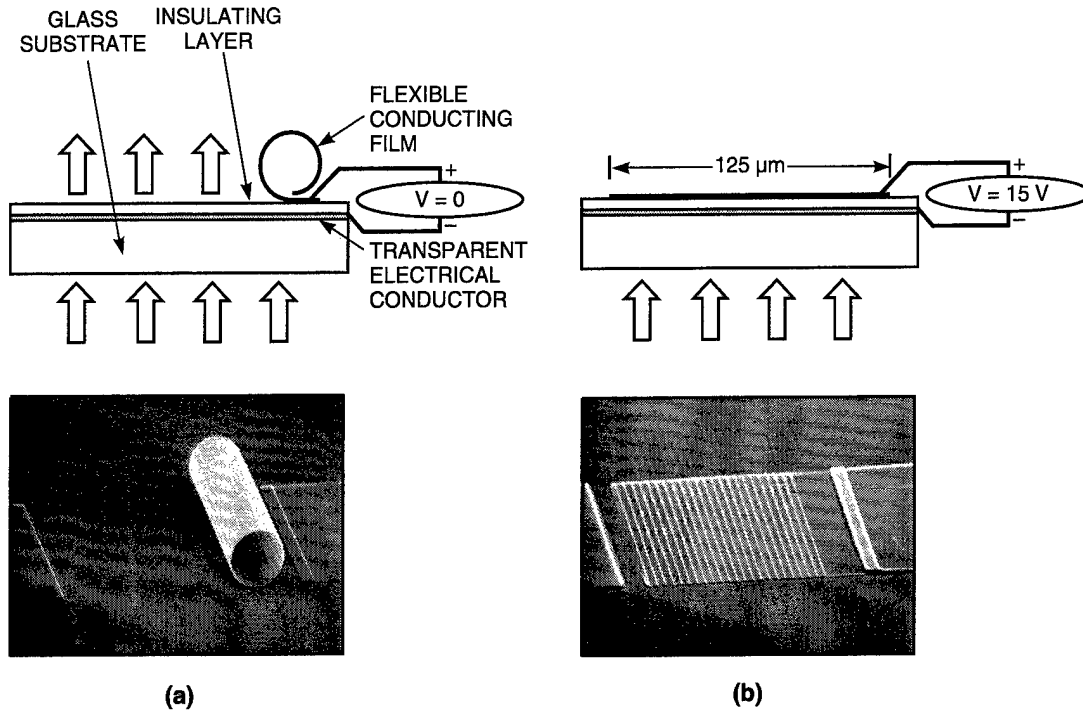
Figure 4-1. Schematics and scanning electron micrographs (SEMs) of microshutter in (a) open and (b) closed positions. By applying a voltage between the flexible conducting film and the transparent conductor, an electric field is created that causes an attractive force. As the voltage is increased the force becomes large enough to overcome the spring force of the flexible conducting film and it rolls out. When the voltage is reduced the spring force causes the film to roll back up.

Many of the processes and equipment used to make microshutters are the same as for other display technologies. Microshutters are made on glass substrates that are patterned with indium tin oxide (ITO), for example. A simplified five-step process is shown in Figure 4-3. Starting with the patterned ITO on glass, photoresist is patterned on the surface of the substrate to provide the release layer. The most critical new part of the process is the formation of the membrane layer over the release layer, which can then be patterned and released from the substrate. The membrane consists of a series of layers designed to have the right built-in stress to cause the coiling when released. After the membrane is patterned, it is released by etching away the photoresist with an oxygen plasma. The coil diameter will be determined by the amount of built-in stress and the membrane thickness. In the past two years we have tried a variety of materials for the membrane and for the release layer, and a variety of release processes.
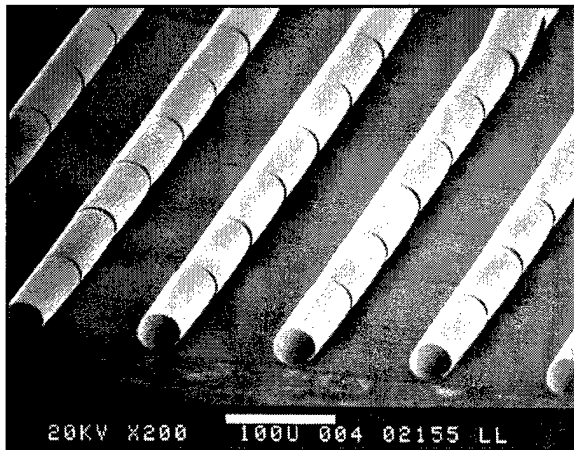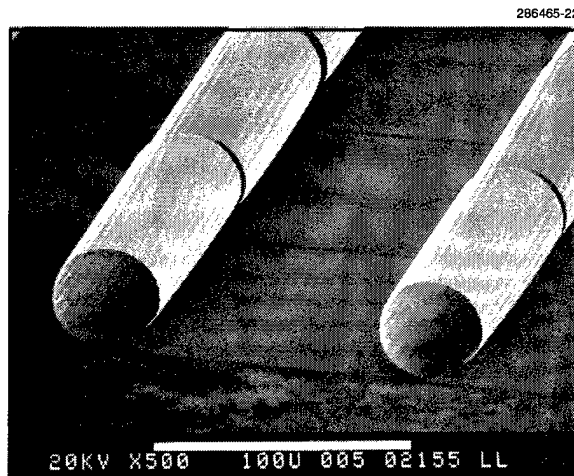
Figure 4-2. SEMs of microshutters in an array used as a display.

We have operated some microshutters at frequencies up to 10 kHz, and one 361-element array to 10^9 cycles with no failures. The power consumption of the microshutter display is determined by the energy flowing in and out of the microshutter capacitance, which is about 10^{-5} W/cm² at 30 Hz. For a 10-in.-square display the power would be 10 mW, which is similar to the power required for an LCD used in a passive mode. In a backlit display the power requirement is around 100 mW, where most of the power goes into the backlight. In the backlit mode the microshutter power consumption will be less than the LCD by a factor of at least 3.
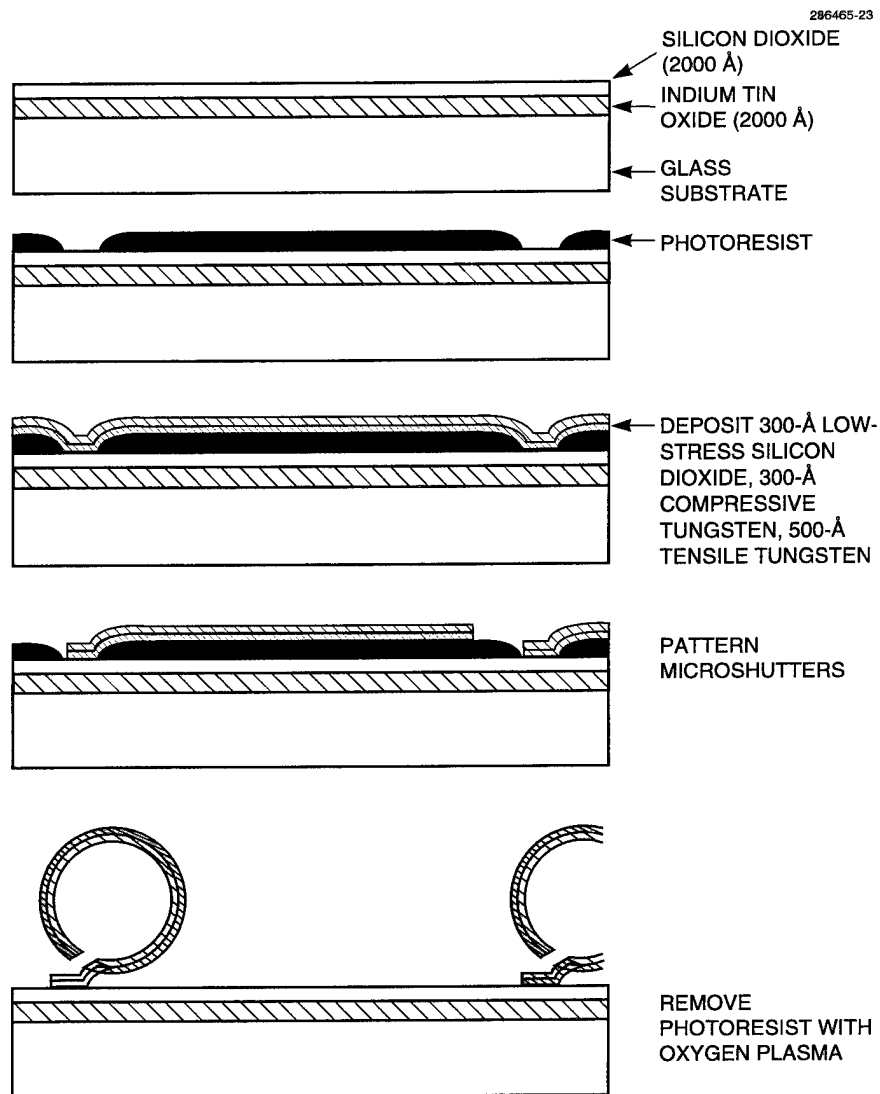
Figure 4-3. Fabrication process for the microshutter device. This is a very simple process that has the potential for very low cost, because there are only four basic steps using commonly available equipment.

This technology is still in a very early stage of development, and we expect it will have a variety of applications—initially for binary images in projection displays and print heads, and later for flat panel displays, both frontlit and backlit, and ultimately with full gray scale and color.

C. O. Bozler
S. Rabe

5. MICROELECTRONICS

5.1 GEIGER-MODE AVALANCHE PHOTODIODE ARRAYS FOR IMAGING LASER RADAR

The performance of an imaging laser radar depends on its time measurement resolution and on a combination of its detection sensitivity and transmitter power. An avalanche photodiode (APD) operated in the Geiger mode (biased above breakdown) can give a fast, large-amplitude signal in response to a single photon. Timing jitter values under 100 ps have been reported [1]. Monolithic APD arrays can be incorporated into lightweight receiver electronics. The gain provided by such sensitive detectors in air-borne laser radar systems can enable substantial reductions in the payload weight and volume required for transmitter components such as laser amplifiers.

We have fabricated monolithic arrays of silicon APDs for operation at 532 nm, and are developing wafer-to-wafer bonding approaches to integrate these arrays with high-speed CMOS timing circuits. One of the most important performance metrics for a Geiger-mode APD is the dark-count rate, which must be low enough to ensure a low probability of a false count during the time interval that the APD is biased above breakdown. We have measured the temperature dependence and bias dependence of the dark count rate for devices in the very first lot of wafers fabricated.

Figure 5-1 illustrates a cross-sectional view of the APD, which is a p^+-p-p-p-n^+ structure formed by epitaxial growth of a 12-μm-thick, lightly boron doped (10^{14} cm^{-3}) silicon layer on a p^+ silicon substrate, followed by ion implantation of boron and arsenic to form the upper p region and the n^+ contact layer, respectively. A phosphorus implant is also done to form a guard ring at the device periphery. The

286465-24
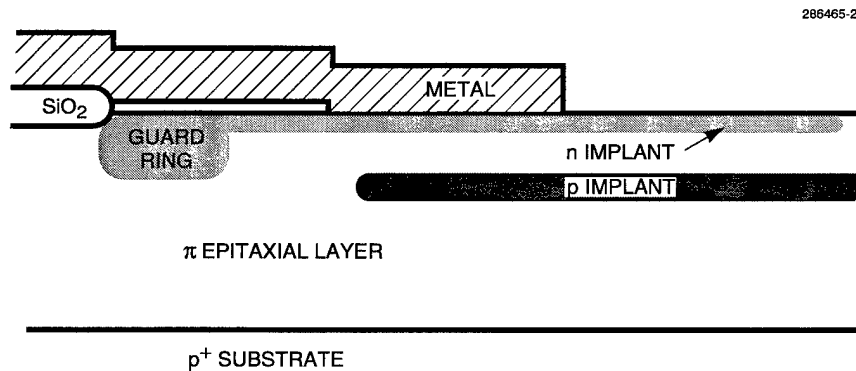
Figure 5-1. Schematic cross section of avalanche photodiode (APD) from periphery to center.
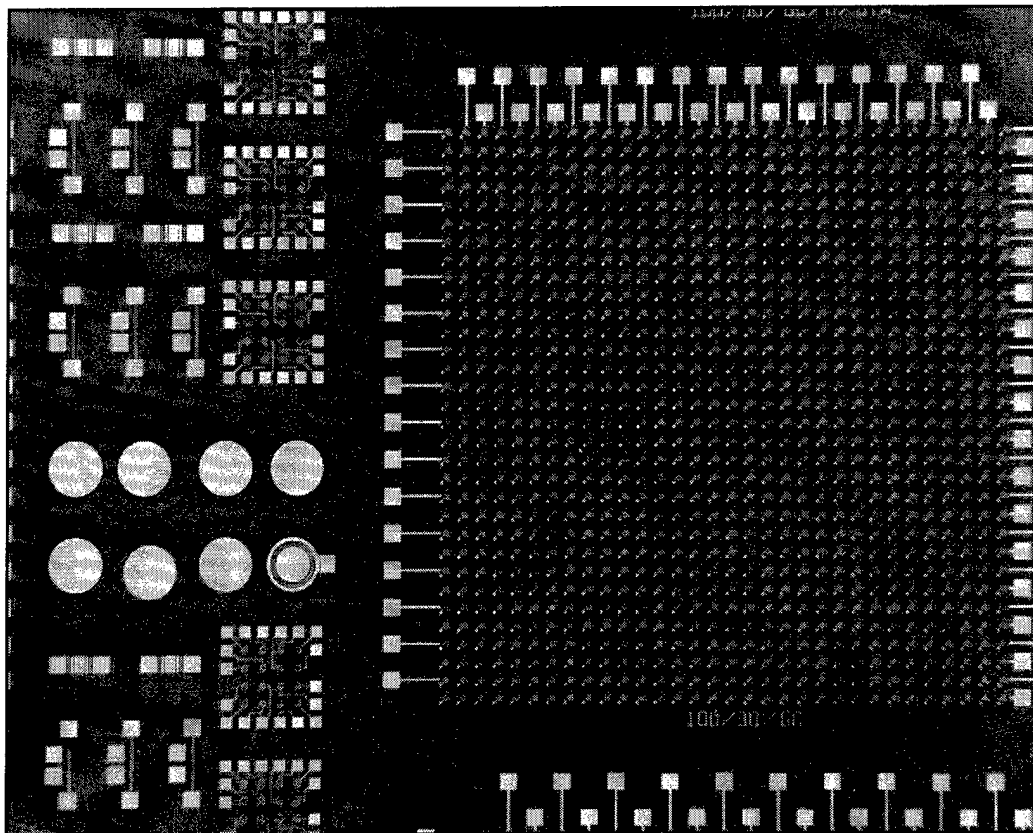
Figure 5-2. Photograph of a portion of a chip. Shown are one 32 × 32 array, several 4 × 4 arrays, and a number of test devices.

lower p layer is for absorption of incident photons, and the upper π layer, which is ~ 0.5 μm thick, is the avalanche region, where photoelectrons initiate impact ionization. The anode contact is formed by metallizing the back side of the wafer. Figure 5-2 shows a photograph of a chip. The entire chip, which is stepped and repeated across a 4-in. wafer, includes eight 32 × 32 and twelve 4 × 4 arrays, along with diagnostic test devices. The devices are circular with active areas of diameters ranging from 20 to 40 μm.

The breakdown voltages of devices in the first six wafers fabricated were typically around 28 V, with a variation of ± 0.4 V over the area of a 4-in.-diam wafer. Figure 5-3 shows the circuit used to characterize APD count rate, both in the dark and in response to an incident photon flux. The APD is charged to some initial bias above the breakdown voltage through a 200-kΩ ballast resistor, and the APD

40

voltage observed with a scope probe. When an avalanche occurs, the APD discharges until its internal fields are no longer sufficient to sustain the avalanche, and then, on a much longer time scale, the APD is charged back up through the ballast resistor. Both the discharge and recharge time constants depend on the total capacitance present across the device, but in our measurement were observed to be ~ 200 ns and 5 μs, respectively. The amplitude of the pulse is commensurate with the amount by which the initial bias exceeds the breakdown voltage, which can be large. The leading edge of the pulse, after buffering through an oscilloscope, was used to trigger a universal counter, thus giving a direct readout of the count rate. Figure 5-4 plots the dark-count rate of a typical device as a function of bias for several temperatures. Typical room-temperature dark-count rates at 32-V bias are in the range 3–5 kHz. At a given bias, the dark-count rate varies exponentially with temperature with activation energies in the range 0.4–0.5 V, indicating that the dark counts are due to carrier generation from midgap trap levels. The count rate increases substantially upon exposure to light, but no calibrated detection probability results are yet available.

The most likely cause of the dark counts is process-related material damage near the device surface, particularly arsenic implantation damage. In subsequent lots of wafers, we are optimizing the fabrication process to ensure that such damage is adequately annealed out.

B. F. Aull

286465-26
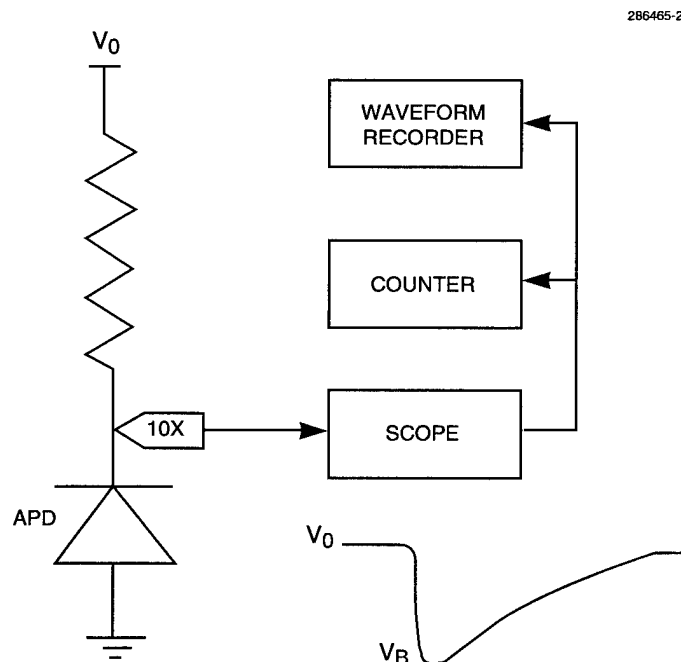
Figure 5-3. APD count rate measurement circuit.

41
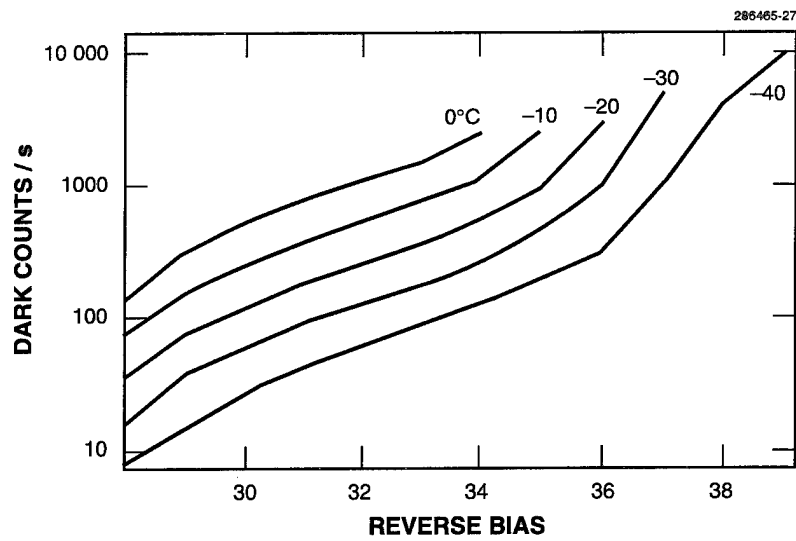
Figure 5-4. Dark count vs bias for a typical device at temperatures ranging from 0 to –40C°.

REFERENCE

1. A. Lacaita, M. Mastrapasqua, M. Ghioni, and S. Vanoli, *Appl. Phys. Lett.* **57**, 489 (1990).

6. ANALOG DEVICE TECHNOLOGY

6.1 MIXED ANALOG-DIGITAL NIOBIUM SUPERCONDUCTIVE CIRCUITS FOR A 2-GIGACHIP-PER-SECOND SPREAD-SPECTRUM MODEM

A 2-gigachip-per-second spread-spectrum modem based on Josephson-junction superconductive electronics is under development [1]–[3]. Using a new doubly planarized all-refractory technology for superconductors (DPARTS) circuit fabrication process, we have recently demonstrated critical subcircuits required to implement the modem. The circuits, which include shift registers and buffers, operate well at frequencies up to 2 GHz, and their performance is in close agreement with simulations.

The functional block diagram of the programmable matched filter for the modem is shown in Figure 6-1. For each bit, or chip (in spread-spectrum terminology), of the spreading code, the filter contains an identical section called a slice. Figure 6-2 shows a block diagram of the first slice along with the output summing and detection circuit. The digital shift registers that control sampling and store the spreading code are implemented using modified variable threshold logic (MVTL) gates [4]. Buffer circuits are required between the shift register outputs and the inputs to the analog cells to provide adequate drive voltages and currents. The output summing bus is implemented by connecting all the taps to a common inductor loop, whose magnetic flux is detected by a quantum flux parametron circuit [5].
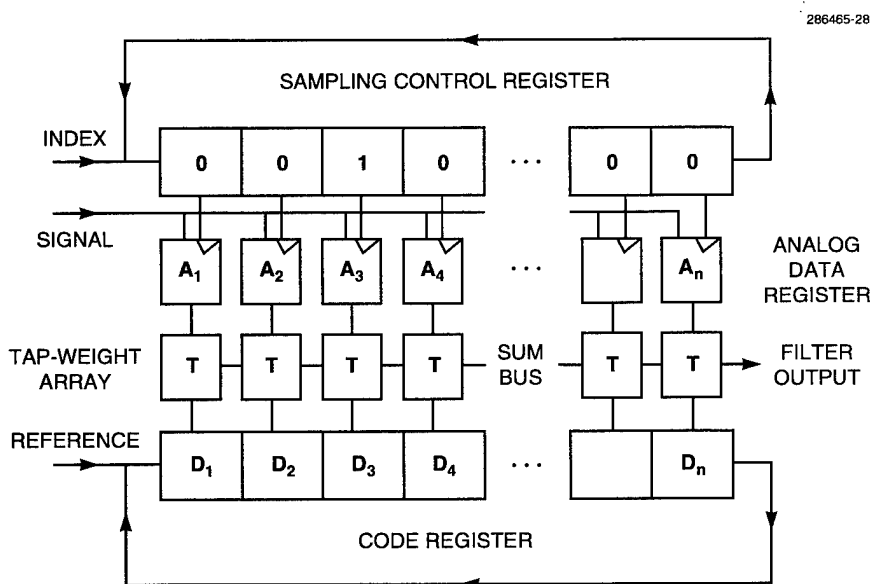
Figure 6-1. Architectural block diagram of high-speed programmable matched filter.
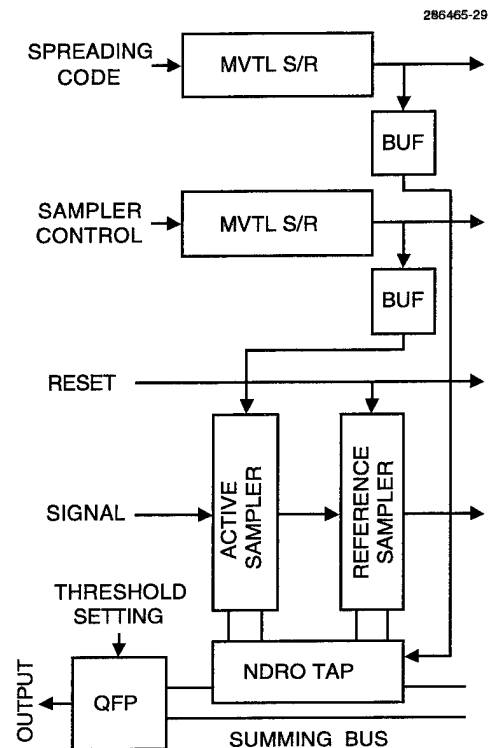
Figure 6-2. Detailed block diagram of one slice of the modem filter with the summing bus and output detector. The diagram shows that the digital shift registers are implemented using modified variable threshold logic (MVTL) gates, that some form of buffer circuit is required between the shift register outputs and inputs to the analog cells, and that the output summing bus is implemented by connecting all the taps to a common inductor loop, whose flux is detected by a quantum flux parametron circuit.

Figure 6-3 shows a simplified circuit schematic for the track/hold (T/H) portion of the filter slice. The digital shift registers, following the design of Meier and Przybysz [6], are intended to operate using three-phase, offset-sine-wave clocks, whose total current into ground is constant to first order, thereby minimizing high-frequency voltage fluctuations in the ground-plane metal (ground bounce). The voltage-amplifying buffer uses stacks of two junctions in series to reach an output level approaching twice the gap voltage, as required to switch the sampler and tap circuits. The two samplers in the T/H cell are designed to be well matched in order to minimize common-mode feedthrough of the input signal, which is applied to both samplers but in opposite directions. The schematic of the tap-weight section of the slice is not shown here but is very similar to Figure 6-3.

The mask set for the modem test circuit run was designed to demonstrate the basic circuit components and to address the interfaces between them. To ensure that the layouts of the subcircuits were consistent with the very tight packing required in the filter, we also included a full filter slice and a complete seven-chip filter. Because of the limited number of pins available on the chips, we could not completely wire up those circuits and could test only parts of them.
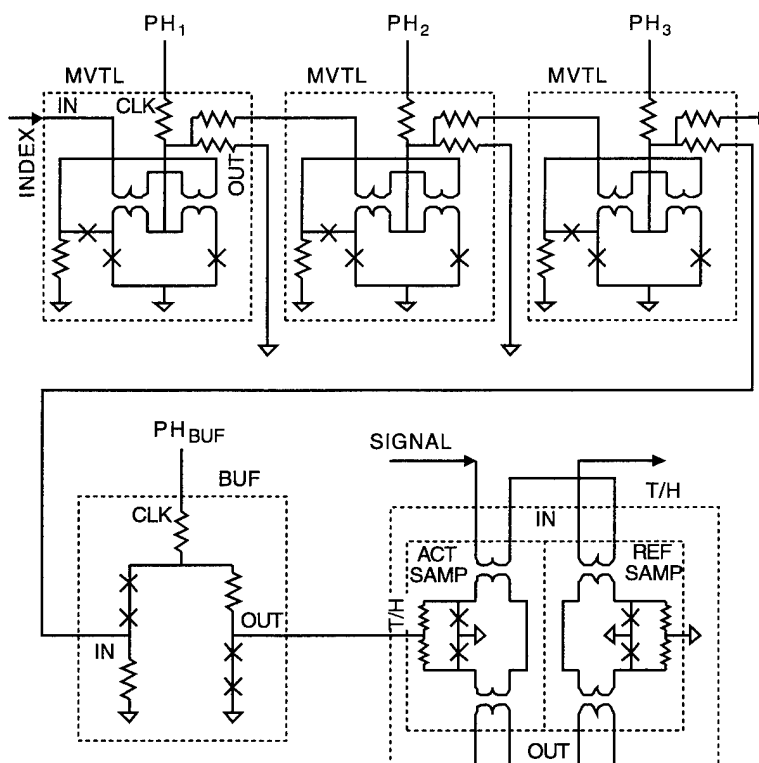
Figure 6-3. Simplified schematic of the track/hold (T/H) portion of the programmable filter.

This mask set included our first implementation of MVTL shift registers. To allow us to characterize the design fully, we included a wide range of test circuits, beginning with just the superconducting quantum interference device (SQUID) that forms the core of the gate. By measuring its characteristics, we could determine the component values in the fabricated circuits. The measured clock margins of a short shift register agreed well with simulations based on those component values.

The MVTL shift register in the complete seven-stage filter prototype was operated first at low frequency with pulse clocks and then at frequencies of 400 MHz and 1 GHz with sine-wave clocks. Because (for lack of pins) the filter had no connection to the shift register input, a trick had to be used to demonstrate its operation. At intervals well in excess of seven clock cycles, the amplitude of a single positive cycle of one clock phase was raised to a level above the MVTL upper clock threshold, causing the gates in every stage of the shift register to switch to the 1 state. The subsequent output from the shift register should be seven 1's followed by 0's. That is exactly what was observed, as shown in Figure 6-4. This result strongly suggests that the shift register should perform well under the operating conditions required in the modem.

286465-32
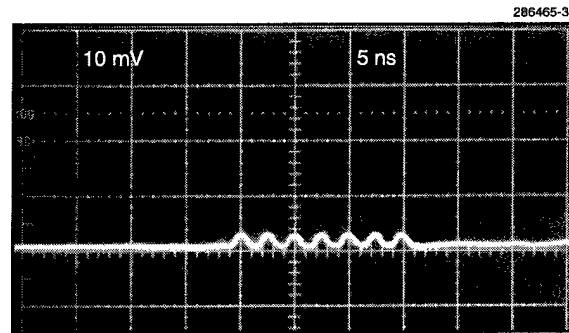
(a)
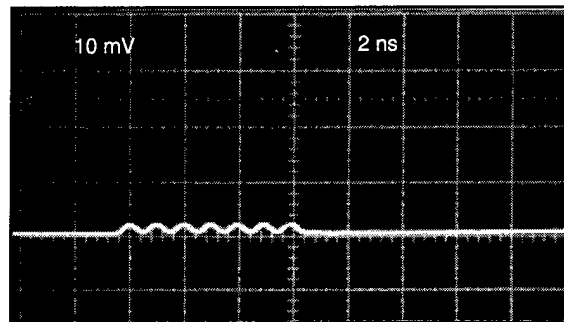
(b)

Figure 6-4. Oscilloscope photographs of the outputs from one of the MVTL shift registers in the complete seven-stage prototype filter when clocked at (a) 400 MHz and (b) 1 GHz.

The buffer subcircuit was also carefully characterized and found to perform as predicted by simulations. The most critical issue with the buffer was whether its output would be strong enough to drive the sampler into track mode. For this purpose, the test chips contained a circuit fragment comprising the buffer and T/H cell shown in Figure 6-3, with a dc SQUID on the T/H output to sense the current stored in the T/H cell. The photograph in Figure 6-5, which shows the output waveforms from the dc SQUID while multiple samples were taken, demonstrates that the T/H was operating under the control of the buffer. The vertical displacement of the trace corresponds to the stored current in the T/H loop, and one can clearly see the expected quantum steps in loop current, given theoretically as Φ_0/L, where Φ_0 is the magnetic flux quantum (2.07 mA pH) and L is the loop inductance of each sampler. The inductance value derived from the measured current step agreed well with the design value.

J. P. Sage
D. A. Feld

46

286465-33

50 mV   50 μV
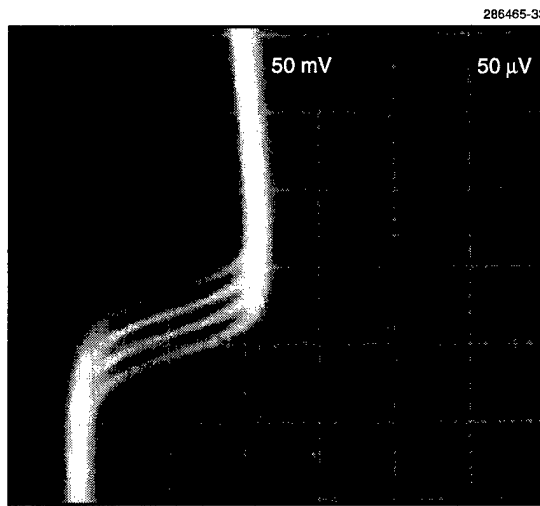
Figure 6-5. Oscilloscope photograph showing a superposition of numerous outputs from the dc superconducting quantum interference device monitoring the samples stored in the T/H cell under command from the buffer circuit. Quantization, as expected, can be seen clearly.

REFERENCES

1. Solid State Research Report, Lincoln Laboratory, MIT, 1994:2, p. 55.

2. J. P. Sage, J. B. Green, and A. Davidson, *IEEE Trans. Appl. Supercond.* **3**, 2562 (1993).

3. J. P. Sage and R. W. Ralston, *Government Microcircuit Applications Conference, 1993 Digest of Papers* (U.S. Army Research Laboratory, Fort Monmouth, N.J., 1993), p. 565.

4. S. Kotani, N. Fujimaki, T. Imamura, and S. Hasuo, *IEEE Trans. Electron Devices* **33**, 379 (1986).

5. Solid State Research Report, Lincoln Laboratory, MIT, 1994:4, p. 33.

6. D. L. Meier and J. X. Przybysz, *IEEE Trans. Appl. Supercond.* **3**, 2736 (1993).

7. ADVANCED SILICON TECHNOLOGY

7.1 SELF-ALIGNED COBALT SILICIDE PROCESS FOR FULLY DEPLETED SILICON-ON-INSULATOR CMOS TECHNOLOGY

Silicon-on-insulator (SOI) MOSFETs with a fully depleted channel in ultrathin (< 50 nm) silicon film have many attractive features in deep submicron gate-length scaling. Among these advantages are improved subthreshold slope, suppression of the floating-body effects, and higher carrier mobility as compared with partially depleted SOI devices. The ultrathin silicon film also results in the reduction of the short-channel effects, which cause the gate to lose channel control with decreasing gate length and prevent scaling into the deep submicron regime. Fully depleted SOI CMOS is therefore a promising technology for high-speed and low-power applications. However, because of the ultrathin silicon film, one major obstacle in implementing this technology is the difficulty in obtaining low source/drain series resistance. A high series resistance can easily offset the advantages to be gained from using the ultrathin SOI material and reduce the circuit speed dramatically. This is especially severe for short-channel devices. To overcome this problem, we have developed and demonstrated a self-aligned cobalt silicide process that can significantly improve the device performance. This process was implemented in the latest 0.25-μm fully depleted SOI CMOS technology (designed for 0.9-V operation) developed at Lincoln Laboratory [1].

Key features of this 0.25-μm gate length SOI CMOS technology include (1) thinning of the SOI layer by oxidation to 50-nm thickness (the buried oxide thickness is 200 nm), (2) mesa island isolation with edge oxide growth and edge implants to reduce sidewall leakage, (3) 8-nm-thick thermally grown gate oxide, (4) dual-doped polysilicon gates for surface channel operation and symmetrical NMOS and PMOS thresholds, (5) source/drain dopant activation by rapid thermal annealing (RTA), (6) 150-nm oxide spacer for the PMOS drift-region formation and the self-aligned cobalt silicide process, (7) TiN/Ti/AlSi/TiN metal stack deposited at 500°C for filling 0.5-μm-wide contacts to silicides.

The design criteria for optimizing the silicide process can be obtained using the transmission line model [2]. This allows one to evaluate the effects of design geometry and silicide quality on the overall source/drain series resistance, which are summarized in the following equations. R_T is the total source/drain series resistance. The spreading resistance from the channel to the source/drain regions and the contact resistance between metal and silicide are neglected in this calculation.

$$R_T = 2R_0 \left\{ 1 + \frac{2\alpha\gamma_{ms}\gamma_s + \alpha\left(\gamma_{ms}^2 + \gamma_s^2\right)\cosh\left(\alpha L_3\right) + \left(\gamma_{ms}\dfrac{R_{ms}}{R_{cf}} + \gamma_s\dfrac{R_s}{R_2}\right)\sinh\left(\alpha L_3\right)}{L_3\left[\left(\alpha^2\gamma_{ms}\gamma_s + \dfrac{R_{ms}R_s}{R_{cf}R_2}\right)\sinh\left(\alpha L_3\right) + \alpha\left(\gamma_{ms}\dfrac{R_s}{R_2} + \gamma_s\dfrac{R_{ms}}{R_{cf}}\right)\cosh\left(\alpha L_3\right)\right]} \right\} , \quad (7.1)$$

where

$$\alpha = \left(\frac{R_{ms} + R_s}{R_c}\right)^{1/2} ; \ \beta = \left(\frac{R_s}{R_c}\right)^{1/2} ; \ \gamma_{ms} = \frac{R_{ms}}{R_{ms} + R_s} ; \ \gamma_s = \frac{R_s}{R_{ms} + R_s} \qquad (7.2)$$

$$R_0 = \frac{L_3}{\dfrac{1}{R_{ms}} + \dfrac{1}{R_s}} ; \ R_1 = \frac{R_{ms} + R_s}{\alpha \tanh\left(\alpha L_1\right)} ; \ R_2 = \frac{R_s}{\beta} \frac{\beta \dfrac{R_1}{R_s} \cosh\left(\beta L_2\right) + \sinh\left(\beta L_2\right)}{\beta \dfrac{R_1}{R_s} \sinh\left(\beta L_2\right) + \cosh\left(\beta L_2\right)} \qquad (7.3)$$

$$R_{ms} = \frac{\rho_{ms}}{W d_{ms}} ; \ R_s = \frac{\rho_s}{W d_s} ; \ R_c = \frac{\rho_c}{W} ; \ R_{cf} = \frac{\rho_{cf}}{W d_c} \ , \qquad (7.4)$$

and the definitions of the various symbols are as follows (also see Figure 7-1 for geometrical symbols): W, gate width; ρ_{ms}, equivalent bulk resistivity of the silicide film in Ω cm; ρ_s, resistivity of the silicon film (Ω cm) in the source/drain regions; ρ_c, specific contact resistivity (Ω cm^2) between silicide and silicon near the bottom interface; and ρ_{cf}, specific contact resistivity (Ω cm^2) between silicide and silicon near the side interface.

286465-34
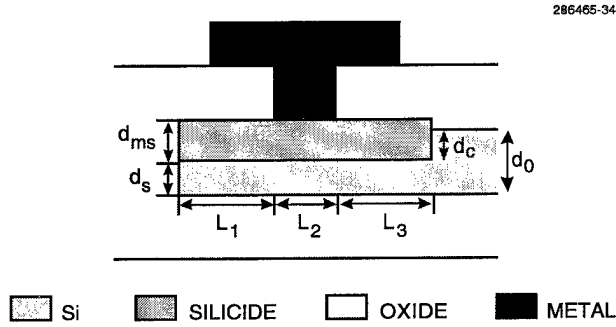
Figure 7-1. Silicide source/drain contact structure. The geometrical parameters illustrated in the figure are used to calculate the source/drain series resistance due to the silicide contact.

In order to minimize its impact on device speed, one would like to have the total source/drain series resistance below 300 Ω μm (normalized to a 1-μm gate width). With this series resistance and a 0.2-μm effective gate length, the current drive of a transistor is already reduced by a factor of nearly 20% compared to the ideal case of zero resistance. This requirement becomes even more stringent as one continues to scale down the gate length.

Because of the ultrathin (50 nm) silicon in the fully depleted SOI process, the effect of the silicide thickness (d_{ms}) will be first investigated. In forming silicide, metal is deposited on silicon and then reacted at high temperature. This chemical process consumes part of the existing silicon layer. For example, a stoichiometric cobalt silicide ($CoSi_2$) consumes 3.64 Å of Si and forms 3.52 Å of $CoSi_2$ for every angstrom of reacted Co. For the more conventional titanium silicide, the corresponding conversion factors are the consumption of 2.27-Å Si and the formation of 2.51-Å $TiSi_2$ for every angstrom of reacted Ti. The silicon consumption increases the sheet resistivity of the underlying Si layer and decreases the effective contact area. This results in a constrained design space plotted in Figure 7-2. For a given specific contact resistivity between the silicide and the Si, there is a required minimum remaining Si thickness to achieve a tolerable series resistance (300 Ω μm in this case). For example, with the 50-nm-thick active layer, a minimum of 20 nm of remaining Si is required for a specific contact resistivity of 5×10^{-7} Ω cm^2. With this condition, it also means that the maximum starting Co film thickness is on the order of 8 nm to assure adequate remaining Si thickness. For Ti silicide, the maximum Ti thickness is ~ 13 nm.

286465-35

$L_1 = L_2 = L_3 = 0.5\mu m$

$d_0 = 50\ nm$

$\rho_{ms} = 25\ \mu\Omega cm$

$\rho_s = 1\ m\Omega cm$
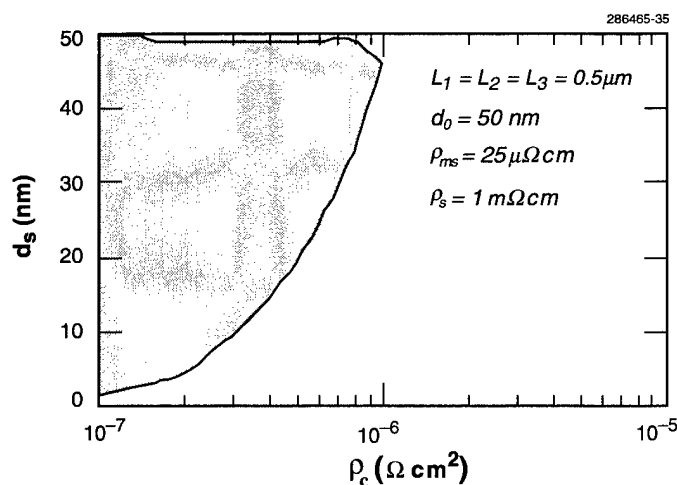
Fgure 7-2. Silicide thickness design space. With the transmission line model, the required remaining silicon thickness (d_s) along with the specific contact resistivity (ρ_c) at the silicide/Si interface are calculated. The shaded area represents possible operating parameters for achieving series resistance < 300 Ω μm.

51

Another important parameter to be investigated is the resistivity of the silicon layer underneath the silicide (ρ_s). Again, the design space for achieving sub-300-Ω μm series resistance is plotted in Figure 7-3. For a specific contact resistivity of 5×10^{-7} Ω cm^2, the required resistivity of the Si layer is < 1 mΩ cm. This condition implies that the doping density needs to exceed 10^{20} cm^{-3}.

Finally, one needs to examine the effects of the silicide sheet resistivity itself. It turns out that in this 50-nm-thick SOI process, the silicide sheet resistivity has little impact on the overall source/drain series resistance. With the same transmission line model and some commonly encountered parameters, the dependence of the series resistance on silicide sheet resistivity is shown in Figure 7-4.
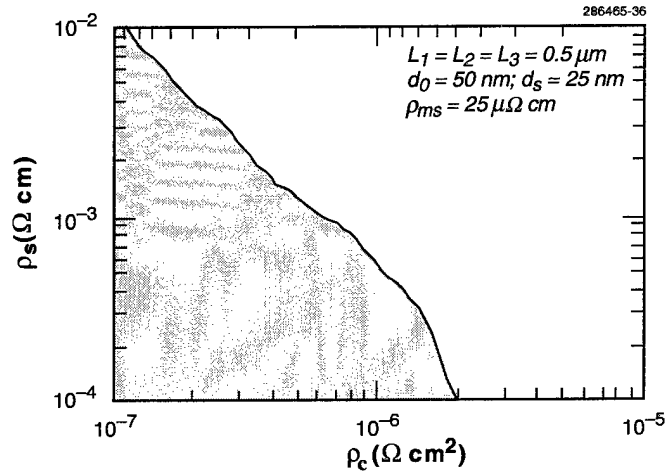
Figure 7-3. Silicon resistivity design space. The required Si resistivity (ρ_s) along with the specific contact resistivity (ρ_c) at the silicide/Si interface are calculated. The shaded area represents possible operating parameters for achieving series resistance < 300 Ω μm.
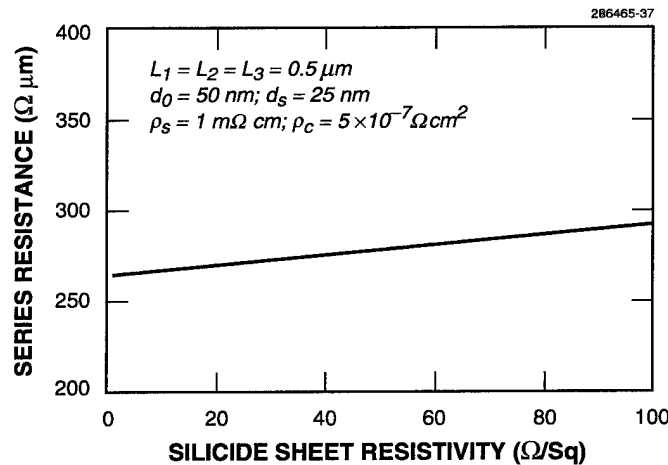
Figure 7-4. Effects of silicide sheet resistivity. The total series resistance is plotted as a function of the silicide sheet resistivity for a set of parameters specified in the chart. It is clear that the dependence is relatively weak.

52

Therefore, one can conclude that in terms of the source/drain series resistance, the dominant parameters are the silicide/silicon specific contact resistivity, the silicide thickness, and the silicon resistivity. Both the specific contact resistivity of the interface and the silicon resistivity are directly related to the dopant density in the silicon layer. To minimize these values, one needs to maximize the degenerate doping in the source/drain regions to the order of 10^{20} cm^{-3}. Although the silicide sheet resistivity plays a less critical role in the source/drain series resistance, it is important to minimize this parameter on the polysilicon gates. Since the silicides are formed simultaneously on the polysilicon gates and the source/drain regions in this self-aligned process, a high sheet resistivity leads to a long RC delay time for gate charging and therefore degrades the circuit performance. The relative importance of the gate-charging delay and the source/drain series resistance still needs to be investigated.

The current cobalt silicide process for the 50-nm-thick fully depleted SOI CMOS technology at Lincoln Laboratory is a two-step RTA process with a Ti capping layer. The entire process flow for the silicide formation is summarized in Table 7-1. Major features of this process include (1) in-situ Ar ion sputtering to eliminate residual native oxide at the Co/Si interface, (2) a 20-nm-thick Ti capping layer on top of the 8-nm-thick Co to improve the Co film stability during the silicide formation, (3) a low-temperature (475°C) first-step RTA to obtain uniform film morphology and prevent bridging between the gate polysilicide and the source/drain silicide. The beneficial role of the capping layer on top of the reacting Co film in improving the silicide film stability and the overall yield has already been clearly demonstrated [3],[4]. However, besides preventing oxidation of the reacting film, other detailed mechanisms responsible for the improvement are still not understood.

TABLE 7-1

Cobalt Silicide Process Flow

Ar ion sputtering to remove 5-nm oxide*
Deposit 8-nm-thick Co by sputtering*
Deposit 20-nm-thick Ti by sputtering*
Rapid thermal anneal (RTA), 475°C, 3 min[†]
Wet etch, 65°C 1:1:1 $NH_4OH:H_2O_2:H_2O$, 90 s
RTA, 700°C, 1 min
*The entire sputter-clean and metal stack deposition process was done in the same chamber without breaking vacuum.
[†]The low temperature greatly eased the removal of the unreacted products in the wet-etch step.

The final silicide films were characterized by several independent experiments. These include (1) four-point probe sheet resistivity measurements on large-area films and on Van der Pauw test structures built into the device wafers, (2) specific contact resistivity measurements by four-point probe on Kelvin test structures, (3) secondary ion mass spectroscopy (SIMS) to determine interface dopant concentration and silicide film thickness, and (4) atomic force microscopy to determine film morphology. The results from these experiments are summarized in Table 7-2.

TABLE 7-2

Ultrathin Cobalt Silicide Characteristics*

Characteristic	Value
$CoSi_2$ sheet resistivity on n^+ Si	16 Ω/sq
$CoSi_2$ sheet resistivity on p^+ Si	13 Ω/sq
$CoSi_2$ sheet resistivity on n^+ poly-Si	16 Ω/sq
$CoSi_2$ sheet resistivity on p^+ poly-Si	14 Ω/sq
Equivalent $CoSi_2$ bulk resistivity	38 $\mu\Omega$ cm
$CoSi_2$ specific contact resistivity to n^+ Si	7×10^{-7} Ω cm^2
$CoSi_2$ specific contact resistivity to p^+ Si	8×10^{-7} Ω cm^2
n^+ (As) dopant concentration at interface	3×10^{20} cm^{-3}
p^+ (B) dopant concentration at interface	2×10^{20} cm^{-3}
n^+ Si resistivity	0.27 mΩ cm
p^+ Si resistivity	1.12 mΩ cm
$CoSi_2$ thickness	25 nm
Si thickness consumed by silicide	26 nm
$CoSi_2$ film rms roughness	1.9 nm

*These characteristics were determined and verified independently by different experiments, listed in the text.

The current process yielded adequate specific contact resistivity between $CoSi_2$ and the underlying Si, on the order of high 10^{-7} Ω cm^2. With these parameters, one expects series resistance of 200 and 400 Ω μm for NMOS and PMOS respectively. These are adequate values for 0.2-μm (gate length) CMOS technology. However, in the current SOI CMOS process, the final silicide films were subjected to a 715°C TEOS deposition process for the contact dielectric. This post-silicide annealing process produces two major problems. First, it degrades the silicide sheet resistivity on n^+ Si and poly by about 30%. This type of thermal instability due to As dopants has also been observed for thicker cobalt silicide films on bulk wafers [5], where it was found that an additional fluorine implant can help in stabilizing the silicide film to withstand a sub-800°C anneal. The other major problem is that the anneal nearly doubles the silicide's contact resistivity to p^+ Si. The additional thermal cycle after the silicide formation is believed to cause boron outdiffusion from the p^+ Si layer. Consequently, one expects a postannealed PMOS series resistance of 720 Ω μm, which is almost a factor of 4 greater than that of an NMOS transistor. A possible solution to improve the PMOS contact resistance is to perform an additional heavy-dose BF_2 implant after the silicide formation. This should replenish the outdiffusion of B during the postanneal. The other, perhaps simpler, alternative is to use a low-temperature oxide deposition process for forming the contact dielectric. Both methods are being aggressively pursued at this time.

Despite the remaining problems with the current cobalt silicide process, it was found to yield high-speed and low-power SOI CMOS circuits. With the current 0.25-μm gate length design rule, the fastest CMOS ring oscillators operate at 28-ps delay per stage and have a power-delay product of 40 fJ at 2 V. Individual transistor characteristics indicate a total source/drain series resistance of 320 Ω μm for NMOS and 1100 Ω μm for PMOS. Some of the discrepancy between these extracted values and the earlier calculated values can be attributed to the spreading resistance from the channel region to the source/drain region, which was not included in the transmission line model.

H. I. Liu   P. W. Wyatt
J. M. Hamm   C. L. Keast
J. A. Burns

REFERENCES

1.   Solid State Research Report, Lincoln Laboratory, MIT, 1996:2, p. 35.

2.   K. Suzuki, T. Tanaka, Y. Tosaka, T. Sugii, and S. Andoh, *IEEE Trans. Electron Devices* **41**, 1007 (1994).

3.   A. C. Berti and V. Bolkhovsky, *1992 VLSI Multilevel Interconnection Conference* (IEEE, Piscataway, N.J., 1992), p. 267.

4.   Q. F. Wang, A. Lauwers, F. Jonckx, M. de Potter, C-C. Chen, and K. Maex, *Mater. Res. Soc. Symp. Proc.* **402**, 221 (1996).

5.   B-S. Chen and M-C. Chen, *IEEE Trans. Electron Devices* **43**, 258 (1996).

REPORT DOCUMENTATION PAGE

Form Approved
OMB No. 0704-0188

1. AGENCY USE ONLY (*Leave blank*)	2. REPORT DATE 15 August 1996	3. REPORT TYPE AND DATES COVERED Quarterly Technical Report, 1 May–31 July 1996

4. TITLE AND SUBTITLE

Solid State Research

6. AUTHOR(S)

David C. Shaver

5. FUNDING NUMBERS

C — F19628-95-C-0002
PE — 63250F
PR — 221

7. PERFORMING ORGANIZATION NAME(S) AND ADDRESS(ES)

Lincoln Laboratory, MIT
244 Wood Street
Lexington, MA 02173-9108

8. PERFORMING ORGANIZATION REPORT NUMBER

1996:3

9. SPONSORING/MONITORING AGENCY NAME(S) AND ADDRESS(ES)

HQ Air Force Materiel Command
AFMC/STSC
Wright-Patterson AFB, OH 45433-5001

10. SPONSORING/MONITORING AGENCY REPORT NUMBER

ESC-TR-96-096

11. SUPPLEMENTARY NOTES

None

12a. DISTRIBUTION/AVAILABILITY STATEMENT

Approved for public release; distribution is unlimited.

12b. DISTRIBUTION CODE

13. ABSTRACT (*Maximum 200 words*)

This report covers in detail the research work of the Solid State Division at Lincoln Laboratory for the period 1 May–31 July 1996. The topics covered are Electrooptical Devices, Quantum Electronics, Materials Research, Submicrometer Technology, High Speed Electronics, Microelectronics, and Analog Device Technology. Funding is provided primarily by the Air Force, with additional support provided by the Army, DARPA, Navy, BMDO, NASA, and NIST.

14. SUBJECT TERMS

quantum electronics	high-speed electronics	optical parametric amplifiers	microchemical etching
electrooptical devices	microelectronics	microlasers	analog-to-digital converters
materials research	analog device technology	lasers	microshutter device
submicrometer technology	advanced silicon technology	epitaxial growth	laser arrays

15. NUMBER OF PAGES
86

16. PRICE CODE

17. SECURITY CLASSIFICATION OF REPORT	18. SECURITY CLASSIFICATION OF THIS PAGE	19. SECURITY CLASSIFICATION OF ABSTRACT	20. LIMITATION OF ABSTRACT
Unclassified	Same as Report	Same as Report	Same as Report